

HALL-EFFECT CONTROLLED GAS DYNAMICS IN PROTOPLANETARY DISKS: I. INNER DISK

XUE-NING BAI¹Institute for Theory and Computation, Harvard-Smithsonian Center for Astrophysics, 60 Garden St., MS-51, Cambridge, MA 02138
Draft version March 3, 2014

ABSTRACT

The gas dynamics of protoplanetary disks (PPDs) is largely controlled by non-ideal magnetohydrodynamic (MHD) effects including Ohmic resistivity, Hall effect and ambipolar diffusion, among which the role of Hall effect is the least explored and most poorly understood. In this series, we have included, for the first time, all three non-ideal MHD effects in a self-consistent manner to investigate the role of Hall effect on the PPD gas dynamics using local shearing-box simulations. In this first paper, we focus on the inner region of PPDs where previous studies of Bai & Stone (2013) and Bai (2013) without including the Hall effect have revealed that the inner disk up to ~ 10 AU is largely laminar with accretion driven by magnetocentrifugal wind. We confirm this basic picture and show that the Hall effect introduces modest modifications to the wind solutions, depending on the polarity of the large-scale poloidal magnetic field \mathbf{B}_0 threading the disk. When $\mathbf{B}_0 \cdot \boldsymbol{\Omega} > 0$, horizontal magnetic field is further amplified, leading to stronger disk wind (by $\sim 50\%$ or less in terms of wind-driven accretion rate). The enhanced horizontal field also leads to much stronger large-scale Maxwell stress that contributes to a considerable fraction of the wind-driven accretion rate. When $\mathbf{B}_0 \cdot \boldsymbol{\Omega} < 0$, horizontal magnetic field is reduced, leading to weaker disk wind (by $\lesssim 20\%$). More importantly, we find that when $\mathbf{B}_0 \cdot \boldsymbol{\Omega} > 0$, the range of stability is enlarged, and one expects the laminar region to extend further to ~ 15 AU before the magneto-rotational instability sets in, while for $\mathbf{B}_0 \cdot \boldsymbol{\Omega} < 0$, the laminar region extends only to ~ 3 AU for typical accretion rate of $\sim 10^{-8} - 10^{-7} M_{\odot} \text{ yr}^{-1}$. Scaling relations for the wind properties, especially wind-driven accretion rate are provided for aligned and anti-aligned field geometries. Implications for global disk evolution and planet formation are also briefly discussed.

Subject headings: magnetohydrodynamics — instabilities — methods: numerical — planetary systems: protoplanetary disks — turbulence

1. INTRODUCTION

The gas dynamics in protoplanetary disks (PPDs) plays a crucial role in essentially every aspect of planet formation. This is mainly because small dust grains are coupled with the gas aerodynamically, while large solids are coupled with the gas gravitationally. What are particularly important include the global structure of the disk, as well as the level of turbulence. For example, the transport and growth of dust grains are sensitive to both the radial pressure gradient and turbulence in PPDs (e.g., Garaud 2007; Birnstiel et al. 2012; Pinilla et al. 2012; Hughes & Armitage 2012), the formation of planetesimals via collective effects such as streaming and gravitational instabilities likely favors regions with small radial pressure gradient and low level of turbulence (e.g. Johansen et al. 2009; Bai & Stone 2010a,b; Youdin 2011), the growth of planetesimals into planetary cores may be suppressed when turbulence is strong which will gravitationally excite their eccentricities, leading to destructive collisions (e.g., Ida et al. 2008; Nelson & Gressel 2010; Yang et al. 2012; Ormel & Okuzumi 2013), and the migration of low to high mass planets, as well as gas accretion onto planetary cores towards giant planet, are all sensitive to the radial disk structure as well as the local microphysics (e.g., Paardekooper et al. 2011; Kretke & Lin 2012; Kley & Nelson 2012; Gressel et al. 2013).

The global structure of the PPDs is bulkly shaped by the process of angular momentum transport, and in the mean time the corresponding mechanism largely dictates the level turbulence in the disk. Therefore, the key in understanding the gas dynamics of PPDs lies in determining the mechanism of angular momentum transport, which is most likely magnetic in nature (see the most recent review by Turner et al. 2014). The most important constraint on such mechanisms comes from the fact that PPDs are actively accreting, with typical accretion rate of $10^{-8 \pm 1} M_{\odot} \text{ yr}^{-1}$ (Hartmann et al. 1998) over the lifetime of about 1-10 Myrs (Sicilia-Aguilar et al. 2006; Ribas et al. 2013), indicating efficient angular momentum transport must take place in the entire disk.

Two leading mechanisms to transport angular momentum in accretion disks include the magnetorotational instability (MRI, Balbus & Hawley 1991) and the magnetocentrifugal wind (MCW, Blandford & Payne 1982). The former generates strong turbulence, which transports angular momentum radially outward within the disk as viscous process (e.g., Shakura & Sunyaev 1973), while the latter extracts angular momentum from the disk vertically, which is then carried away by the wind. The details about whether and how these mechanisms operate in PPDs largely depend on how the gas and magnetic field are coupled inside the disk, as well as the geometry of the magnetic field.

Fully ionized gas can generally be well described by ideal magnetohydrodynamics (MHD) where conductivity is infinity hence the gas and magnetic field are perfectly

xbai@cfa.harvard.edu
¹ Hubble Fellow

coupled, while extremely weakly ionized gas applicable in PPDs is subject to three non-ideal MHD effects, namely, Ohmic resistivity, Hall effect, and ambipolar diffusion (AD). These non-ideal MHD effects weaken the coupling between gas and magnetic fields in different ways, leading to reduced level of the MRI turbulence or even fully suppress the MRI (Fleming et al. 2000; Sano & Stone 2002b; Bai & Stone 2011). They also strongly affect the launching process of the MCW (Wardle & Koenigl 1993; Königl et al. 2010; Salmeron et al. 2011).

With calculations of ionization-recombination chemistry to infer the level of ionization in PPDs, it is clear that all three non-ideal MHD effects are relevant and important in PPDs (Wardle 2007; Bai 2011a). In particular, Ohmic resistivity dominates in high densities with weak magnetic field ($\eta_O \propto x_e^{-1}$, where x_e is the ionization fraction), applicable to the midplane region of the inner disk ($\lesssim 10$ AU), AD dominates in low density regions with strong magnetic field ($\eta_A \propto x_e^{-1} B^2 / \rho^2$), applicable to the surface region of the inner disk, as well as the bulk of the outer disk ($\gtrsim 100$ AU). The Hall-dominated regime lies in between ($\eta_H \propto x_e^{-1} B / \rho$), which covers a large fraction of PPDs, particularly the planet-forming regions.

The role of Ohmic resistivity has been the major focus for most works in the literature, and has led to the standard picture of layered accretion (Gammie 1996), followed by more than a decade of further developments using numerical simulations with increasing level of complexity (e.g., Fleming & Stone 2003; Turner & Sano 2008; Hirose & Turner 2011). These works have firmly established that the MRI does not operate in the midplane region of the inner disk due to the excessively large resistivity, which is termed as the dead zone. While Hall effect and AD are progressively more important towards disk surface, they were not included in these studies and the surface region was found as expected to be fully MRI turbulent (resistivity completely negligible) and is termed as the active layer.

Ambipolar diffusion (AD) is the second non-ideal MHD effect that receives considerable attention. Non-linear simulations of the MRI with AD (Bai & Stone 2011, in the “strong-coupling” limit applicable to weakly ionized gas) showed that in the AD dominate regime, the MRI operates only when magnetic field is sufficiently weak with reduced level of turbulence. This finding led Bai (2011a,b) and Perez-Becker & Chiang (2011b,a) to conclude that MRI is insufficient to drive rapid accretion at the observed rate of $10^{-8} M_\odot \text{ yr}^{-1}$ by at least one order of magnitude, at least in the inner disk.

Recently, it has been demonstrated that when both Ohmic resistivity and AD are taken into account with self-consistent treatment of ionization-recombination chemistry, MRI is either extremely inefficient or completely suppressed (depending on magnetic field geometry) in the inner part of PPDs (Bai & Stone 2013b; Bai 2013). While this result seems surprising, it is consistent with theoretical expectations, because the conventional “active layer” is AD dominated, and AD at disk surface is strong enough to disable the MRI. Without the MRI, accretion is found to be driven very efficiently by the MCW, and the desired rate of $10^{-8} M_\odot \text{ yr}^{-1}$ can be easily achieved when the disk is threaded by some weak

net vertical magnetic field. Towards the outer disk where AD is expected to be the sole dominant non-ideal MHD effect, MRI is able to operate, but to achieve sufficient accretion rate, again net vertical magnetic flux is essential (Simon et al. 2013b,a). These results are pointing to a paradigm shift in our understanding of the gas dynamics in PPDs, highlighting the importance of MCW and external large-scale magnetic field.

The Hall effect is the last non-ideal MHD effect yet to be included in self-consistent models of PPDs. It has been shown to strongly affect the the linear properties of the MRI (Wardle 1999; Balbus & Terquem 2001; Wardle & Salmeron 2012). Non-linear simulations which included both Ohmic resistivity and Hall effect indicated that the Hall term changes the saturation level of the MRI (Sano & Stone 2002a,b), and the effect can be more dramatic when much stronger Hall coefficient is included (Kunz & Lesur 2013). The Hall effect also affect the wind launching process hence the properties of the magnetic wind, as studied in detail in Königl et al. (2010) and Salmeron et al. (2011) extending the early work of Wardle & Koenigl (1993). These authors identified the wind launching criteria in the presence of all three non-ideal MHD effects separated in different regimes and presented representative wind solutions. These works provided important theoretical framework for the general behavior of the wind solution, though main limitations involve unrealistic assumptions of constant Elsasser numbers (of order unity) and strong vertical magnetic field (near equipartition at midplane).

A special consequence of the Hall effect is that it makes the gas dynamics depend on magnetic polarity: reversing the magnetic field would violate the original dynamical equations hence a different configuration is required. Since the Hall effect is prominent in a wide range of disk radii, the gas dynamics of PPDs is largely Hall-controlled, and one expects it to bifurcate into two branches with different field configurations and flow properties depending on the polarity of the large-scale magnetic field.

This paper, together with the companion paper, represent the first effort to explore the role of Hall effect in PPDs using non-linear MHD simulations with self-consistent treatment of the ionization-recombination chemistry. They serve as an extension of the recent work by Bai & Stone (2013b) and Bai (2013) by further including the Hall effect. In this first paper, we focus on the inner part of the disk ($R \lesssim 10$ AU) where MRI is expected to be suppressed in the entire disk. We show that the conclusion that the MRI is suppressed with MCW-driven accretion still holds, while the property of the MCW is different and depends on the polarity of the external large-scale magnetic field. In the companion paper, we focus to the outer region of the disk and address how the behavior of the MRI is affected by the Hall effect.

This paper is organized as follows. Given the increasing level of complexity compared with previous works, especially involving the full non-ideal MHD physics, we devote Section 2 for background information to guide the readers through the formulation and the role played by individual non-ideal MHD effects, highlighting the new features introduced by the Hall term. Section 3 describes

the methodology of our numerical simulations as well as the simulation runs. In Section 4, we focus on a particular set of simulations with fiducial parameters and discuss how the Hall effect modifies the original wind solution obtained by Bai & Stone (2013b) and the properties of the new wind solutions. We then extend the results with a much broader range of parameters in Section 5. In Section 6 we discuss the implications of our findings and conclude.

2. PRELIMINARIES

2.1. Disk Model

We plan to study the local gas dynamics of PPDs across a wide range of disk radii. Since we are interested in short time scales (~ 100 local orbital time) compared with disk lifetime, we adopt a fixed disk model without worrying about the global disk evolution. As a convention, we use the minimum-mass solar nebular (MMSN) disk as our standard model, with surface density and temperature given by (Weidenschilling 1977; Hayashi 1981)

$$\begin{aligned}\Sigma(R) &= 1700 R_{\text{AU}}^{-3/2} \text{ g cm}^{-2}, \\ T(R) &= 280 R_{\text{AU}}^{-1/2} \text{ K}.\end{aligned}\quad (1)$$

where R_{AU} is disk radius measured in AU. We treat the disk as vertically isothermal, with isothermal sound speed given by $c_s = 0.99 R_{\text{AU}}^{-1/4} \text{ km s}^{-1}$ (mean molecular weight $\mu = 2.34 m_p$). While in reality the disk is hotter at the surface and colder in the midplane due to stellar irradiation, we are mainly interested in the role played by magnetic fields which is likely the primary driving force of disk angular momentum transport, and we leave more realistic treatment of thermodynamics for future work.

2.2. Formulation

We study the gas dynamics in PPDs using the standard local shearing-sheet approximation (Goldreich & Lynden-Bell 1965), where MHD equations are written in the Cartesian coordinate in the corotating frame at a fiducial radius R with Keplerian frequency Ω . With the inclusion of non-inertial forces (Coriolis force and tidal gravity in both radial and vertical directions), the equations in cgs units read

$$\begin{aligned}\frac{\partial \rho}{\partial t} + \nabla \cdot (\rho \mathbf{u}) &= 0, \\ \frac{\partial \mathbf{u}}{\partial t} + (\mathbf{u} \cdot \nabla) \mathbf{u} &= -\frac{\nabla P}{\rho} + \frac{\mathbf{J} \times \mathbf{B}}{c\rho} + 2\mathbf{u} \times \boldsymbol{\Omega} + 3\Omega^2 x \mathbf{e}_x - \Omega^2 z \mathbf{e}_z,\end{aligned}\quad (2)$$

where ρ , \mathbf{u} , P are the gas density, velocity and pressure respectively, \mathbf{B} is the magnetic field, $\mathbf{J} = (c/4\pi)\nabla \times \mathbf{B}$ is the current density, $\mathbf{e}_x, \mathbf{e}_y, \mathbf{e}_z$ are unit vectors pointing to the radial, azimuthal and vertical directions respectively, where $\boldsymbol{\Omega}$ is along the \mathbf{e}_z direction. We use an isothermal equation of state with $P = \rho c_s^2$, where c_s is the isothermal sound speed. Note that we have included the vertical gravity of the central object, hence there is density stratification. In hydrostatic equilibrium, the gas density follows hydrostatic profile of $\rho = \rho_0 \exp(-z^2/2H^2)$, where ρ_0 is the midplane gas density, and $H \equiv c_s/\Omega$ is the disk scale height. The background Keplerian shear

flow is determined by the balance of the Coriolis force and the radial tidal gravity, with $\mathbf{u}_0 = -(3/2)\Omega x \mathbf{e}_y$, and we use

$$\mathbf{v} \equiv \mathbf{u} + \frac{3}{2}\Omega x \mathbf{e}_y \quad (4)$$

to denote deviations from background shear.

For very weakly ionized gas as in PPDs, the above single-fluid equations describe the dynamics for the bulk of the neutral gas. Note that the neutral gas also feels the Lorentz force, which is effectively achieved since charged particles (which directly feel the Lorentz force) frequently collide with the neutrals.

The charged particles contain negligible inertia, and in the dense environment of PPDs (collision frequency with the neutrals is much higher than orbital frequency), their dynamics is fully determined by the balance between the Lorentz force and collisional drag with the neutrals. In this so-called “strong coupling” limit, multi-fluid equations are unnecessary. The motion of charged particles simply provides the conductivity for the bulk of the gas, which is generally anisotropic due to the presence of magnetic field. Reflecting to the induction equation, such anisotropic conductivity introduces three non-ideal MHD effects in addition to the normal inductive term

$$\begin{aligned}\frac{\partial \mathbf{B}}{\partial t} &= \nabla \times (\mathbf{u} \times \mathbf{B}) - c \nabla \times \mathbf{E}' \\ &= \nabla \times (\mathbf{v} \times \mathbf{B}) - \frac{3}{2} B_x \Omega \mathbf{e}_y - c \nabla \times \mathbf{E}',\end{aligned}\quad (5)$$

with

$$c\mathbf{E}' \equiv \frac{4\pi}{c} [\eta_O \mathbf{J} + \eta_H (\mathbf{J} \times \hat{\mathbf{B}}) + \eta_A \mathbf{J}_\perp], \quad (6)$$

where \mathbf{E}' is the electric field (in the comoving frame) due to non-ideal MHD terms, $\hat{\mathbf{B}}$ denotes unit vector along \mathbf{B} , subscript “ \perp ” denotes the vector component that is perpendicular to \mathbf{B} , η_O, η_H and η_A are the Ohmic, Hall and the ambipolar diffusivities. For future convenience, we further define the total electric field as

$$\mathbf{E} = -(\mathbf{v}/c) \times \mathbf{B} + \mathbf{E}'. \quad (7)$$

The general expression of these diffusivities involve knowledge on the abundance of all charged species (Wardle 2007; Bai 2011a), but in the absence of small charged grains, the diffusivities can be cast into particularly simple form:

$$\begin{aligned}\eta_O &= \frac{c^2 m_e \gamma_e \rho}{4\pi e^2 n_e} \propto \left(\frac{n_H}{n_e} \right), \\ \eta_H &= \frac{cB}{4\pi e n_e} \propto \left(\frac{n_H}{n_e} \right) \left(\frac{B}{\rho} \right), \\ \eta_A &= \frac{B^2}{4\pi \gamma_i \rho \rho_i} \propto \left(\frac{n_H}{n_e} \right) \left(\frac{B}{\rho} \right)^2.\end{aligned}\quad (8)$$

where n_H is the number density of the hydrogen nuclei, γ_e and γ_i denote the coefficient of momentum transfer during electron-neutral and ion-neutral collisions (see Bai 2011a), n_e is the electron number density and ρ_i is the ion mass density. As a common practice, we define

n_e/n_H as the ionization fraction. Under this circumstance (which is commonly applicable), Ohmic resistivity describes the collisions between the electrons and the neutrals, the Hall term describes the electron-ion drift $\mathbf{v}_e - \mathbf{v}_i$, and the AD term describes the ion-neutral drift $\mathbf{v}_i - \mathbf{v}$. We further see that the strength of all three effects is inversely proportional to the ionization fraction n_e/n_H , while their dependence on (B/ρ) reveal that Ohmic resistivity (independent of B/ρ) dominates in dense regions with weak magnetic field, AD dominates in sparse regions with strong magnetic field, and the Hall-dominated regime lies in between.

The importance of these non-ideal MHD effects in PPDs can be characterized by defining the Elsasser numbers for each of the terms

$$\Lambda \equiv \frac{v_A^2}{\eta_O \Omega}, \quad \chi \equiv \frac{v_A^2}{\eta_H \Omega}, \quad Am \equiv \frac{v_A^2}{\eta_A \Omega} \approx \frac{\gamma_i \rho}{\Omega}, \quad (9)$$

where $v_A = \sqrt{B^2/4\pi\rho}$ is the Alfvén velocity. The non-ideal MHD terms become dynamically important when any of these Elsasser numbers become much smaller than 1, while the ideal MHD limit applies when they largely exceed 1. Note that Am is independent of magnetic field strength, and in the absence of small grains, it corresponds to the number of times a neutral molecule collides with the ions in a dynamical time (Ω^{-1}).

2.3. Hall Effect and Characteristics

The effects of Ohmic resistivity and AD have been extensively studied in the literature. Here we elaborate on the characteristics of the Hall effect, which is the focus of this work.

Working with Equation (8) for magnetic diffusivities, we can first define the Hall frequency as

$$\omega_H \equiv \frac{en_e B}{m\rho c} = \frac{\rho_i}{\rho} \omega_i, \quad (10)$$

where $\omega_i = eB/m_i c$ is the gyro-frequency of the ions. Therefore, the Hall frequency is simply the ion gyro-frequency reduced by the level of ionization. With this definition, the Hall Elsasser number is simply given by

$$\chi = \frac{\omega_H}{\Omega}. \quad (11)$$

The Hall effect is not dissipative because the Hall electric field $\mathbf{E}'_H \propto \mathbf{J} \times \mathbf{B}$ which is perpendicular to \mathbf{J} , hence $\mathbf{E}'_H \cdot \mathbf{J} = 0$. Instead of dissipation, the Hall effect breaks the degeneracy between left and right polarized Alfvén waves. The left-handed wave does not propagate beyond ω_H , while the right-handed wave (the whistler wave) has the asymptotic dispersion relation of $\omega \propto k^2$ at $\omega \gg \omega_H$ (see Appendix B and Equation (B2)). The Hall effect is therefore important on timescales comparable to or shorter than ω_H^{-1} , where the whistler wave physics comes into play. Since the gas dynamics in PPDs is characterized by the dynamical timescale Ω^{-1} , we see that the Elsasser number very well characterizes the importance of the Hall term which plays a significant role when $\chi \lesssim 1$.

The Hall term also introduces a characteristic length

scale l_H (Kunz & Lesur 2013)

$$l_H \equiv \frac{v_A}{\omega_H} = \left(\frac{\rho}{\rho_i}\right) \left(\frac{v_A}{\omega_i}\right) = \left(\frac{\rho}{\rho_i}\right)^{1/2} \left(\frac{c}{\omega_{pi}}\right), \quad (12)$$

where the Hall effect is important on scales smaller than l_H . It is the analog of the ion inertia length (or ion skin depth) c/ω_{pi} in fully ionized plasma, enlarged by the square root of (ρ/ρ_i) , where $\omega_{pi} = \sqrt{4\pi n_i e^2/m_i}$ is the ion plasma frequency. It is useful to normalize l_H by the disk scale height H , which gives

$$\frac{l_H}{H} = \sqrt{\frac{2}{\beta}} \frac{1}{\chi}, \quad (13)$$

where the plasma β is defined as the ratio of gas pressure to magnetic pressure, or $2c_s^2/v_A^2$. The Hall effect is expected to strongly influence the gas dynamics of the disk when $l_H \gtrsim H$.

We note that while ω_H is proportional to the magnetic field strength, l_H is independent of magnetic field strength and is fully determined by the level of ionization ($l_H \propto \rho/\rho_i$). Therefore, l_H/H provides a very useful dimensionless measure on the strength of the Hall term, with $\eta_H = l_H v_A$.

Unlike Ohmic resistivity and AD, the effect of the Hall term depends on magnetic polarity. In the induction equation (5), if one reverses the magnetic field, the Hall term does not change sign while all other terms do (since $\mathbf{J} \propto \nabla \times \mathbf{B}$), hence the Hall term breaks the magnetic reversal symmetry which holds broadly in ideal/resistive/AD MHD². In PPDs, this means that different field configurations are expected when the external magnetic field is aligned or anti-aligned with $\mathbf{\Omega}$. In other words, the gas dynamics in PPDs is expected to be different for different orientations of the large-scale magnetic flux. For our choice, the aligned and anti-aligned cases correspond to net $B_z > 0$ and $B_z < 0$ in shearing-box simulations.

2.4. MRI Suppression and Disk Wind Launching

The focus of this paper is the inner part of PPDs, where we expect the suppression of the MRI and launching of disk wind. The two facts are closely related, and depend on the amount of external net vertical (poloidal) magnetic flux threading the disk. Let $B_0 = |B_z|$ be the strength of the net vertical field, and it is best characterized again by the parameter β_0

$$\beta_0 \equiv \frac{P_{g,\text{mid}}}{P_{B0}} = \frac{\rho_0 c_s^2}{B_0^2/8\pi}. \quad (14)$$

Here we use subscript ‘0’ to specifically denote the net (or background) vertical field. The plasma β defined using total field strength can be much smaller.

In the ideal MHD limit, MRI operates efficiently for $\beta_0 \gtrsim 100$ (Bai & Stone 2013a). Zero net vertical flux (or $\beta_0 \rightarrow \infty$) leads to relatively weak turbulence

² In the shearing-sheet approximation, a steady-state wind solution is always invariant under the transformation $\mathbf{B}_h \rightarrow -\mathbf{B}_h$, $\mathbf{v}'_h \rightarrow -\mathbf{v}'_h$, where subscript ‘h’ denotes the horizontal component. Without the Hall term, the wind solution is also invariant under $B_z \rightarrow -B_z$, $\mathbf{v}'_h \rightarrow -\mathbf{v}'_h$.

with Shakura-Sunyaev $\alpha \sim 0.02$ (e.g., Davis et al. 2010; Shi et al. 2010). Increasing the net vertical flux leads to stronger turbulence with larger α (see definition (25)), and the level of turbulence saturates at $\beta_0 \sim 10^2 - 10^3$, giving $\alpha \sim 1$ (Bai & Stone 2013a). Further increasing the net vertical flux would stabilize the MRI, which is not expected to operate for $\beta_0 \lesssim 10$ (e.g., Latter et al. 2010; Lesur et al. 2013).

Non-ideal MHD effects modify the properties of the MRI in different ways. For Ohmic resistivity, the MRI has been shown to operate when $\Lambda \gtrsim 1$ (e.g., Turner et al. 2007; Ilgner & Nelson 2008). In the inner region of PPDs, it turns out that Ohmic resistivity is always excessively large for the MRI to operate at disk midplane region (e.g., Gammie 1996; Ilgner & Nelson 2006; Bai & Goodman 2009). For AD, MRI can always operate in the presence of net vertical magnetic field but weaker magnetic field is required for stronger AD (see Fig. 16 of Bai & Stone 2011). With numerical simulations, Bai & Stone (2013b) and Bai (2013) found that it is only possible for the MRI to operate when the net vertical magnetic flux is extremely weak ($\beta_0 \gtrsim 10^6$), or is completely vanishing. The resulting level of turbulence is orders of magnitude too small to efficiently drive disk accretion.

To some extent, the main difference between fully ionized disks and the inner part ($\lesssim 10$ AU) of PPDs is that the threshold for the suppression of the MRI switches from a strong field $\beta_0 \sim 10$ to a very weak field $\beta_0 \sim 10^6$ because of the strong non-ideal MHD effects.

From local shearing-box simulations of the MRI, it was found that the presence of net vertical magnetic flux always leads to the launching of a disk outflow (e.g., (Suzuki & Inutsuka 2009; Okuzumi & Hirose 2011; Fromang et al. 2013; Bai & Stone 2013a). The outflow is magnetocentrifugal in nature (Blandford & Payne 1982), but it is unclear whether it connects to a global magnetocentrifugal wind mainly because the MRI dynamo activities render the radial orientation of the outflow to oscillate (Bai & Stone 2013a). Most recent global MRI simulations that include net vertical magnetic flux are still inconclusive on the fate of such disk outflow due to limited vertical domain size and other numerical issues (Suzuki & Inutsuka 2013).

The launching of a steady disk wind generally requires the presence of strong net vertical field with $\beta_0 \sim 1$ (e.g., Wardle & Koenigl 1993; Ferreira & Pelletier 1995), which is also found to be the case from local steady state wind solutions that include all non-ideal MHD effects (Königl et al. 2010; Salmeron et al. 2011). However, these conditions are all derived by assuming constant magnetic diffusivities or constant Elsasser numbers and the wind is essentially launched from the disk interior. More appropriately, launching of disk wind only requires equipartition field at the wind launching region (e.g., Li 1996; Wardle 1997). In the inner region of PPDs, the disk interior is essentially decoupled with magnetic field due to the excessively large Ohmic resistivity, hence magnetic wind launching is only possible from disk surface layer where gas and magnetic fields are better coupled. Equipartition field at the low density disk surface corresponds to much larger β_0 , and indeed, we found that when properly include Ohmic resistivity and AD,

a steady wind can be naturally launched with $\beta_0 \sim 10^5$ (Bai & Stone 2013b; Bai 2013).

In brief, the strong non-ideal MHD effects in the inner region of PPDs makes the launching of steady disk winds much easier, and can be achieved with very weak net vertical field. This is closely related to the suppression of the MRI discussed earlier since MRI is the main source that prevents the launching of steady wind.

2.5. Structure and Symmetry of the Wind Solution

The wind solutions presented in this paper extend earlier wind solutions of Bai & Stone (2013b) and Bai (2013) by including the Hall term. These wind solutions share many common properties which we briefly summarize below.

The wind launching process (see Figure 6 and Section 4.1 of Bai & Stone 2013b) first involves the build up of a relatively strong toroidal field in the disk interior. Toward the disk surface, the toroidal field is reduced in strength, driving a current in the radial direction. The radial motion of the charge carriers associated with this current then drag and bend magnetic field lines radially. Upon achieving the critical inclination angle of 30° about disk normal, the wind is launched magnetocentrifugally (Blandford & Payne 1982). For the laminar wind solution, we can divide the vertical extent of the disk into a disk zone containing the disk midplane where the azimuthal gas velocity is sub-Keplerian, and a wind zone at disk surface where the azimuthal velocity is super-Keplerian. The height at which this transition occurs, z_b , is referred to as the base of the wind (Wardle & Koenigl 1993).

The wind carries away disk angular momentum, and the rate of which is determined by the $z\phi$ component of the stress tensor $T_{z\phi}$ at the base of the wind z_b (Bai & Stone 2013b)

$$T_{z\phi}^{z_b} = -\frac{B_z B_y}{4\pi} \Big|_{\pm z_b} \quad (15)$$

Note that only the Maxwell (magnetic) component is involved, because the Reynolds (hydrodynamic) component is simply zero by the definition of z_b . The value of z_b is typically found to be around $4H$ or higher.

The total rate of angular momentum loss from the disk is given by the difference of the above stress at the top and bottom side of the disk $\pm z_b$. Note that B_z is constant through the disk, hence to have net angular momentum loss, B_y must change sign across the disk. This desired symmetry of the magnetic field is the even- z symmetry, where $B_x(z) = -B_x(-z)$ and $B_y(z) = -B_y(-z)$, and the radial component of the field bends to the same direction at the top and bottom sides of the disk. Correspondingly, the rate of wind-driven accretion is given by

$$\dot{M}_V = \frac{8\pi}{\Omega} R |T_{z\phi}^{z_b}| \approx 4.1 \times 10^{-8} M_\odot \text{ yr}^{-1} \left(\frac{|T_{z\phi}^{z_b}|}{10^{-4} \rho_0 c_s^2} \right) R_{\text{AU}}^{-3/4}, \quad (16)$$

where subscript 'v' represents accretion is driven by vertical angular momentum transport, and in the latter estimate, we have adopted the MMSN disk model, with R_{AU} being disk radius normalized to AU.

In numerical simulations containing both sides of the

disk, it was found that the simulations sometimes generate solutions with odd- z symmetry ($B_x(z) = B_x(-z)$, $B_y(z) = B_y(-z)$), which is unphysical with the radial field at the top and bottom sides bending to opposite radial directions. This is mostly due to the limitation of the shearing-box framework, where disk curvature is ignored hence there is no distinction between radially inward or outward. The physical solution can be obtained by flipping the horizontal field at one side of the disk. However, the physical solution does not strictly obey the even- z symmetry: the flip does not exactly take place at the disk midplane, but at some height above through a thin layer. This is because the midplane region is too resistive to conduct electric current, and only in the upper layer (typically at $z \sim 1 - 3H$) can the flip take place where there is marginal coupling between gas and magnetic field (see section 4.4 of Bai & Stone 2013b for more discussions). The thin layer carries a strong current due to the flip of the horizontal field, it also receives the entire Maxwell stress from the wind and possesses large radial velocities. In reality, this layer should carry the entire accretion flow (Bai & Stone 2013b), although global disk simulations are required to address the stability and radial structure of this strong current layer.

Despite the issue with the symmetry of the wind solution, it was found that the solution in the wind zone, in particular, $T_{z\phi}^{z_b}$, is independent of such symmetry (see Section 4.4.1 of Bai & Stone 2013b for details). This is mainly because z_b is typically much higher than the location where horizontal field flips. For this reason, if we are mainly interested in the properties of the disk wind, it suffices to enforce the even- z symmetry in numerical calculations, by simulating half of the disk ($z \geq 0$) with $B_x(z=0) = B_y(z=0) = 0$.

3. SIMULATION SETUP AND PARAMETERS

3.1. Methodology

We use ATHENA, a higher-order Godunov MHD code with constrained transport technique to enforce the divergence-free constraint on the magnetic field (Gardiner & Stone 2005, 2008; Stone et al. 2008) for all calculations presented in this paper. Non-ideal MHD terms including Ohmic resistivity (Davis et al. 2010), and AD (Bai & Stone 2011) have been developed for Athena. In this work, we have further implemented the Hall term, with detailed algorithms described in Appendix A, with code tests shown in Appendix B. Following the formulation in Section 2.2, all our simulations are carried out using the shearing-box module with orbital advection (Stone & Gardiner 2010), and a zero-gradient outflow boundary condition with hydrostatic density profile (Simon et al. 2011). We always adopt natural unit in the simulations with $\rho_0 = c_s = \Omega = 1$. While we write down the formulas in Gauss unit, in the code magnetic fields are rescaled such that magnetic permeability $\mu = 1$ (e.g., magnetic pressure is $B^2/2$).

Most our simulations are quasi-1D along the vertical dimension of the disk to construct laminar wind solutions. They are quasi-1D because we use a three-dimensional (3D) simulation box with only 4 cells in the horizontal dimensions. The additional horizontal dimensions were found to be necessary for our time-dependent

simulation to properly relax to the laminar wind configuration (Bai & Stone 2013b). The vertical domain covers half of the disk, extending from $z = 0$ to $z = 8H$. As discussed in Section 2.5, this is sufficient to capture the desired wind solution without complications by issues involving symmetry and the strong current layer, which may not be properly handled in the shearing-box framework. In the vertical direction, we use a resolution of 24 cells per H , which was also found to be sufficient to properly resolve the wind structure.

The magnetic diffusivities η_O , η_H and η_A are obtained self-consistently in the simulations based on a pre-computed look-up table assuming equilibrium chemistry. For η_H and η_A , they are given in η_H/B and η_A/B^2 which are independent of B for the regimes we consider in this paper (in the absence of abundant small grains). Since we adopt the MMSN disk model with isothermal equation of state, the diffusivity table is two-dimensional providing the diffusivities as a function of density and ionization rate at fixed temperature. The ionization rate includes contributions from stellar X-ray, cosmic rays and radioactive decay, are expressed a function of column density to the disk surface (see Section 3.2 of Bai 2011a), where fiducially we adopt X-ray luminosity of $L_X = 10^{30}$ erg s $^{-1}$ and X-ray temperature of 5 keV 3 . The procedure closely follows the description in Bai & Stone (2013b), with some changes and updates described below.

We have updated our chemical reaction network with the most recent version of the UMIST database (McElroy et al. 2013). Reactions are extracted using the same list of chemical species adopted in our previous works (Bai & Goodman 2009; Bai 2011a,b; Bai & Stone 2013b; Bai 2013), which originated from the work of Ilgner & Nelson (2006). The total number of gas-phase reactions increases from 2083 to 2147. The grain-binding energy of all species are also updated to the new values. We have tested the new chemical network and found that for a grain-free calculation, the new network gives ionization fractions that are typically slightly smaller compared with the previous version, but within a factor of 2. Fiducially, we include a single population of dust grains with size $a = 0.1\mu\text{m}$ and abundance of 10^{-4} in mass, which is the same as used in our earlier works (Bai & Stone 2013b; Bai 2013). While this is by no means realistic, it provides reasonable and representative amount of total surface area to enhance recombination. It has been shown that the properties of the wind solution depend very weakly on the grain abundance (Bai & Stone 2013b), mainly because the wind is launched from disk upper layers where ionization fraction \gg grain abundance.

The disk surface layer is also exposed to far-UV (FUV) radiation which greatly enhances the level of ionization (which is not captured in our diffusivity table) so that the gas behaves in the ideal MHD regime. In our previous works (Bai & Stone 2013a; Bai 2013), we obtained the diffusivities in the FUV layer separately by assuming constant ionization fraction of $\sim 10^{-5} - 10^{-4}$, and the FUV layer was assumed to have a penetration depth of $0.01 - 0.1$ g cm $^{-2}$ based on the work by

³ The X-ray ionization calculation has been updated recently by Ercolano & Glassgold (2013) who found results consistent with previous calculations of Igea & Glassgold (1999) which we adopt.

Perez-Becker & Chiang (2011a). Correspondingly, there is a sharp jump of diffusivities across the FUV ionization front (lower left panel of Figure 5 in Bai & Stone 2013b). More self-consistent X-ray and UV radiative-transfer calculations (e.g., Walsh et al. 2010, 2012) showed that the ionization fraction increases smoothly from disk midplane to the disk upper layer. To avoid unrealistic sharp transitions, in this work, we empirically treat the FUV ionization as another independent ionization source, with ionization rate of

$$\xi_{\text{FUV}} = 1.0 \times 10^{-6} R_{\text{AU}}^{-2} \exp(-\Sigma/\Sigma_{\text{FUV}}) \text{s}^{-1}. \quad (17)$$

The ionization is assumed to act on hydrogen and helium in the same way as X-ray and cosmic-rays so that we can simply use the diffusivity table by extending it to higher ionization rates. This assumption is by no means physical (FUV ionization does not act on H or He), but it works for our purpose since we simply need a prescription to allow the gas to behave in the ideal MHD regime in the FUV layer with a smooth transition, and the detailed ionization structure in the FUV layer is unimportant. To further validate this choice, we have calculated the ionization profiles at 1, 10 and 100 AU based on the above ionization rate at disk surface, and compared the results with the radiative transfer and chemistry calculations of Walsh et al. (2012) with the same X-ray luminosity and temperature⁴. We find reasonable agreement when $\Sigma_{\text{FUV}} \approx 0.005 \text{ g cm}^{-2}$, which will be the standard value we adopt in this paper.

From our chemistry calculations, the magnetic diffusivities at the disk midplane can become excessively large, leading to excessively small timesteps from the Courant condition. Besides using super time-stepping to handle Ohmic resistivity and AD (see Appendix A), we further set a diffusivity floor $\eta_{\text{fr}} = 10c_s H$ so that $\eta_O + \eta_H + \eta_A \leq \eta_{\text{fr}}$. If the floor value is reached, the values of η_O , η_H and η_A are reduced proportionally so as not to affect their relative importance. We have carefully verified that this floor value is sufficiently large and the properties of our wind solutions are independent of η_{fr} .

3.2. Simulation Runs

Our simulations mainly have two parameters, namely, the radial location in the disk R , and the net vertical magnetic field B_z characterized by β_0 (with vertical field aligned with $\mathbf{\Omega}$). For each combination of the two parameters, we have three simulation runs. We begin by including only the Ohmic resistivity and AD, which sets the benchmark following our previous works (Bai & Stone 2013b; Bai 2013). This run is continued to time $t = 480\Omega^{-1}$, where the system has fully settled into the laminar configuration. We then turn on the Hall term and split the simulation into two more runs: one is continued from the first run, where $B_z > 0$ for aligned vertical field, and for the other we flip all three components of the magnetic field so that it becomes anti-aligned with $\mathbf{\Omega}$, while keeping the velocities unchanged. These simulations are run for another ~ 80 orbits to $t = 960\Omega^{-1}$

which is sufficient for the system to relax to a new wind solution.

Our simulation runs mentioned above are named as run $RxbyH*$, where x represents disk radius in AU, $y = \log_{10} \beta_0$, and $*$ can be 0, ‘+’, ‘-’ for the initial simulation without the Hall term (0), the continued simulation including the Hall term with $B_{z0} > 0$ (‘+’) and $B_{z0} < 0$ (‘-’), respectively. For instance, our fiducial runs focused in the next section, R1b5H+ and R1b5H-, are fixed at $R = 1\text{AU}$ with $\beta_0 = 10^5$. For these fiducial runs R1b5H*, we further perform a set of runs with variations in other parameters, and the results will be addressed in Section 5.1. The list of the fiducial runs and their variations are provided in Table 1, where the latter are labeled by attaching additional letters in front of the standard run names. We consider disk masses that are 3 and 0.3 times the MMSN disk, labeled by ‘M3’ and ‘M03’. We also perform runs with grain-free chemistry, labeled by ‘nogr’. Finally, we vary the X-ray ionization rate to $L_X = 10^{29}$ and $10^{31} \text{ ergs s}^{-1}$, labeled by ‘X29’ and ‘X31’. In the remaining of Section 5, we further consider runs with $\beta_0 = 10^4$ and 10^6 , and R at 0.3, 3, 5, 8 and 15 AU, where all other parameters are fixed with standard values. The list of these simulation runs are provided in Table 2.

4. SIMULATION RESULTS: REPRESENTATIVE WIND SOLUTIONS

We begin by focusing on a fiducial set of simulation runs at fixed radius of 1 AU with $\beta_0 = 10^5$. In Figure 1, from left to right, we show the general properties of the wind solutions for runs R1b5H-, R1b5H0 and R1b5H+ respectively. Major diagnostic quantities of these solutions are provided in Table 1. The rest of this section is devoted to discussing the properties of these solutions.

4.1. Relaxation to New Wind Solutions

We start from the middle panels of Figure 1 for run R1b5H0, where the Hall term was not included. The solution closely resembles the fiducial solution in our previous work Bai & Stone (2013b) (see their Figures 5, 11 for solutions with odd and even symmetries), except that the Elsasser number profile in this work smoothly transitions towards the surface FUV layer as a result of the new procedure adopted in this work. While the penetration depth of the FUV layer is uncertain, such smooth transition is likely more realistic.

We divide this solution into three parts. The first part covers the midplane region up to $z \sim 2.5H$. This region is highly resistive, and the coupling between gas and magnetic field is very weak, hence the horizontal field remain close to zero (due to enforced even- z symmetry). The second part ranges from $z \sim 2.5$ to the base of the wind $z \sim 4.5H$, where with reduced resistivity the gas is marginally coupled to the magnetic field. The third part is the wind zone (beyond the wind base), where the gas behaves approximately in the ideal MHD regime and simply responds passively to the wind launched from below. The gas dynamics in the first two regions are strongly controlled by the Hall effect, and we discuss below how the inclusion of the Hall effect leads the solution R1b5H0 to the other new solutions R1b5H \pm .

Let us focus on the second part $z \sim 2.5 - 4.5H$. With the addition of the Hall term, the original solution no

⁴ We sincerely acknowledge H. Nomura and C. Walsh for rerunning their calculations with new parameters and providing us the data for comparison.

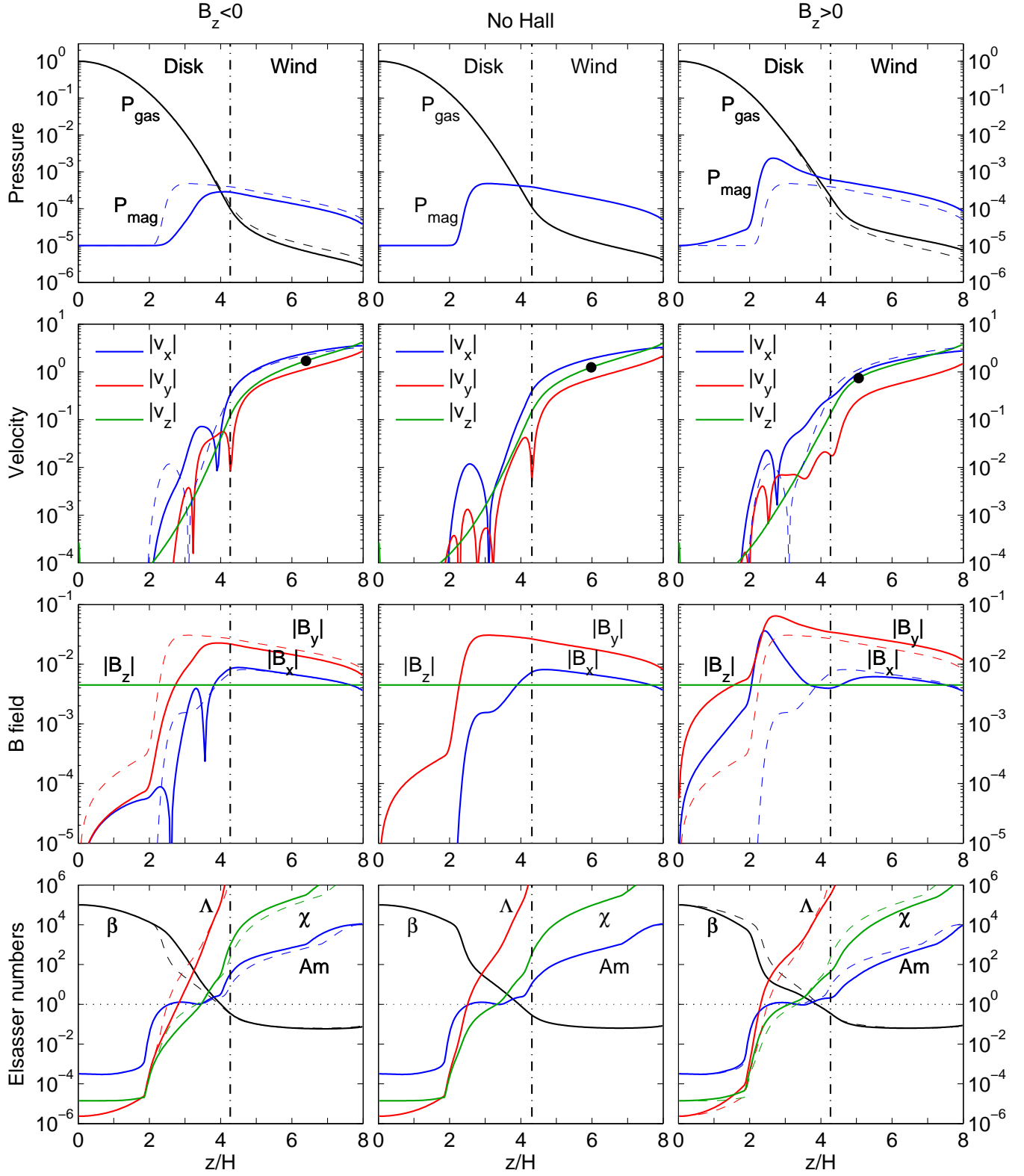


FIG. 1.— Vertical profiles of various quantities in the laminar wind solutions from our fiducial simulations ($R=1\text{AU}$, $\beta_0 = 10^5$), where reflection symmetry about the midplane is enforced for physical wind solutions. Left panels: solution with $B_z < 0$ (solid lines). Middle panels: solution without including the Hall effect. Right panels: solution with $B_z > 0$ (solid line). Top row: gas and magnetic pressure; second row: three velocity components, where the black dot marks the Alfvén point; third row: three magnetic field components; bottom row: Ohmic, Hall and AD Elsasser numbers, as well as the total plasma β . For comparison, we also show the solution without including the Hall effect in dashed lines in the left and right panels (but only $|v_x|$ in the second row to avoid confusion). In all panels, the vertical dash-dotted line marks the location of the base of the wind $z = z_b$. Velocity and magnetic field components are shown for absolute values. For velocities, all components are positive in the wind zone, the sign changes every time the curve transitions through a kink in the logarithmic plot. For magnetic fields, B_x , $-B_y$ and B_z have the same sign in the wind zone. Note the sign of B_x flips twice in the $B_z < 0$ simulation.

longer satisfies the induction equation, and the immediate evolution of magnetic field should follow

$$\begin{aligned}\frac{\partial B_x}{\partial t} &= \eta_{Hz} \frac{\partial^2}{\partial z^2} B_y, \\ \frac{\partial B_y}{\partial t} &= -\eta_{Hz} \frac{\partial^2}{\partial z^2} B_x - \frac{3}{2} \Omega \Delta B_x,\end{aligned}\quad (18)$$

where η_{Hz} is the Hall diffusivity based on the vertical magnetic field and contains the sign of B_z , assumed to be constant to facilitate the analysis, and ΔB_x represents changes in B_x to account for additional shear conversion of B_x to $-B_y$ (middle term on the right hand side of Equation (5)).

When $B_z > 0$, we have $B_x > 0$ and $B_y < 0$ in the original solution of R1b5H0. Since $|B_y|$ is several times larger than B_x , the strongest evolution takes place on B_x due to the second derivative of B_y . The latter is maximized at the peak of $|B_y|$ at around $z = 3H$, where we find $\partial B_x / \partial t > 0$. Therefore, we expect strongest amplification of B_x around that location, which is indeed observed on the right panel of Figure 1. The strong amplification of B_x further enhances the shear conversion of B_x into $-B_y$, hence $|B_y|$ is also amplified. This largely explains why B_y is stronger in the solution R1b5H+. When B_x is sufficiently amplified, which produces a hump around $z \sim 2.5H$, the second of the above equations indicate $\partial B_y / \partial t > 0$. Since $B_y < 0$, this hump in B_x suppresses the further shear amplification of $|B_y|$.

When $B_z < 0$, we have $B_x < 0$ and $B_y > 0$ using the flipped version of the original solution R1b5H0, and also $\eta_{Hz} < 0$. Again using the above equations, we find $\partial B_x / \partial t > 0$ at the peak of B_y (around $z = 3H$). Since $B_x < 0$, and given the small value of $|B_x|$ and large second derivative of B_y , the Hall effect drives B_x to change sign from negative to positive. This explains the kinks in the logarithmic plot of B_x in the left column of Figure 1. The reversal of B_x also leads to the reduction of B_y , but not to reverse it, because AD is taking over to balance the shear conversion of B_x .

In our time-dependent simulations, the relaxation from the original solution of R1b5H0 to the new solutions R1b5H \pm is very rapid, as we show in Figure 2. The initial evolution of B_x takes much less than an orbit, with a few more orbits to fully relax to the final configuration.

The qualitative behaviors of the new solutions discussed above are very general since they are just based on the simple fact that the $|B_y|$ has a single maxima (which gives large second derivative) at certain height above the disk midplane. The existence of this maxima is undoubted because $|B_y|$ has to be built up and then smoothly decrease to launch the wind (see Section 2.5). The location of this peak generally corresponds to the region above the midplane where the gas and magnetic field becomes marginally coupled (Ohmic and AD Elsasser numbers get to above order unity), and can be regarded as the starting point of the wind is launching process⁵.

In brief, for $B_z > 0$, the inclusion of the Hall effect en-

hances the magnetic field strength. This effectively enhances the coupling between the gas and magnetic field (i.e., increased Ohmic and Hall Elsasser numbers) and allows the magnetic field to be amplified deeper towards disk interior. For $B_z < 0$, the Hall effect tends to reduce the magnetic field strength and leads to the reversal of B_x in the disk interior. Correspondingly, the gas can be considered as less coupled to the magnetic field and magnetic field amplification occurs at higher surface layers.

4.2. Midplane Field Configuration

Next we focus on the magnetic field configuration in the disk interior ($z \lesssim 2H$). Our discussion is mainly based upon the framework set up in earlier works of Wardle & Koenigl (1993) and Königl et al. (2010).

We consider the radial and azimuthal components of the Euler equation (3). For a steady-state 1D solution, the force balance gives

$$\begin{aligned}v_z \frac{dv_x}{dz} &= \frac{J_y B_z}{c\rho} + 2v_y \Omega \approx 0, \\ v_z \frac{dv_y}{dz} &= -\frac{J_x B_z}{c\rho} - \frac{1}{2} v_x \Omega \approx 0,\end{aligned}\quad (19)$$

where the last approximate equality holds near the disk midplane, because the vertical velocity there is largely zero and the wind is launched from much higher regions.

We next consider the induction equation (5). For a steady state solution, it essentially reduces to

$$\frac{d(cE_x)}{dz} = -\frac{3}{2} B_r \Omega, \quad (20)$$

and

$$E_y = E_{y0}, \quad (21)$$

where E_{y0} is a constant independent of z . Physically, E_{y0} corresponds to the rate of radial transport of magnetic flux, with radial drift velocity given by $v_{Bx} \equiv cE_{y0}/B_z$. In our time-dependent shearing-box simulations, its value is related to the way vertical boundary condition is implemented. In our earlier work of Bai & Stone (2013b) without the Hall term, we found that our solution gives $E_{y0} \approx 0$, though non-zeros values were found in some other simulations with different vertical boundary conditions (e.g. Lesur et al. 2013)⁶. Similarly, let E_{x0} be the value of E_x at $z = 0$. Then $v_{By} \equiv -cE_{x0}/B_z$ corresponds to the effective midplane drift velocity of magnetic flux, and one expects $v_{By} < 0$ (sub-Keplerian) for a physical wind solution (Königl et al. 2010).

For our representative wind solutions at 1 AU, we see that within $\sim 2H$ about the disk midplane, Ohmic resistivity and the Hall term are the dominant non-ideal MHD effects. For our analysis here, we therefore ignore the contribution from the AD term in Equation (6), which gives

$$\begin{aligned}cE_x &= \frac{4\pi}{c} (\eta_O J_x + \eta_{Hz} J_y) - v_y B_z, \\ cE_{y0} &= \frac{4\pi}{c} (\eta_O J_y - \eta_{Hz} J_x) + v_x B_z,\end{aligned}\quad (22)$$

⁵ In Bai & Stone (2013b), this location is referred to as the wind launching point. Note that in their unphysical odd- z symmetry solutions, $|B_y|$ maximizes, B_y is flat across the midplane, but the second derivative of B_y peaks at the wind launching point.

⁶ They generally have discontinuities in magnetic fields across the vertical boundaries.

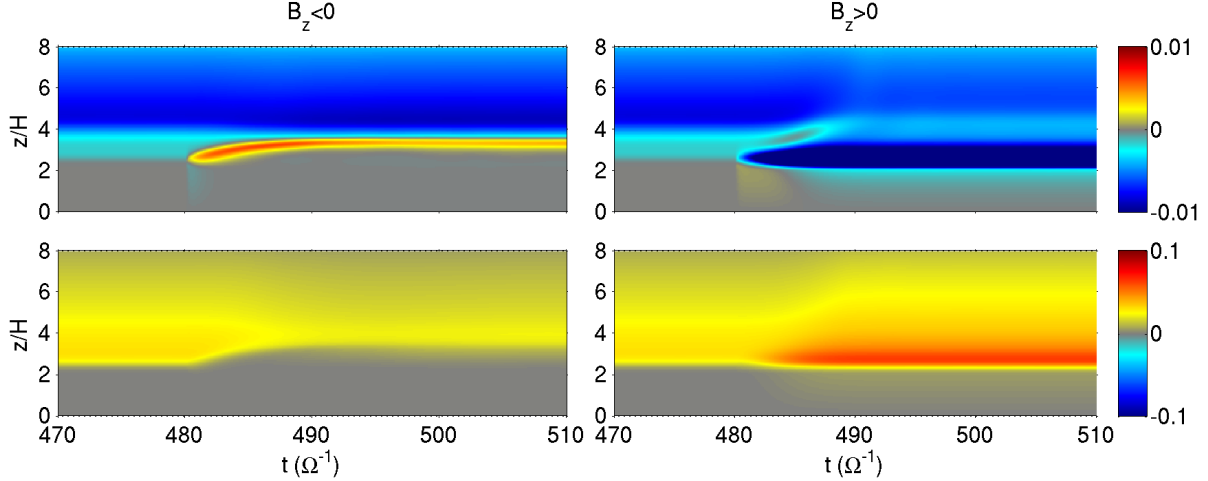


FIG. 2.— Time evolution of the magnetic field profile B_x (upper panels) and B_y (lower panels) around the time the Hall effect is turned on at $t = 480\Omega^{-1}$. Left and right panels correspond to cases with $B_z < 0$ and $B_z > 0$ respectively, where we have properly flipped the magnetic field in the case of $B_z < 0$ to enable more direct comparison.

where η_{Hz} is the Hall diffusivity using the z -component of the magnetic field. Substituting Equation (19) into the above, we obtain

$$\begin{aligned} \frac{cE_x}{B_z} &= -\frac{v_x}{2\Lambda_z} - \frac{2v_y}{\chi_z} - v_y, \\ \frac{cE_{y0}}{B_z} &= -\frac{2v_y}{\Lambda_z} + \frac{v_x}{2\chi_z} + v_x, \end{aligned} \quad (23)$$

where Λ_z and χ_z are the Ohmic and Hall Elsasser numbers based on the z -component of the magnetic field. Also note that χ_z has the same sign as B_z .

Let us assume that $v_{Bx} = cE_{y0}/B_z \approx 0$, then we have $v_x/v_y \approx 4\chi_z/[\Lambda_z(1 + 2\chi_z)]$. Since $v_x \propto -2J_x \propto 2dB_y/dz$, $v_y \propto -J_y/2 \propto (-dB_x/dz)/2$, therefore, we find $dB_x/dB_y \approx -\Lambda_z(1 + 2\chi_z)/\chi_z$. This is a generic result applicable to regions near the disk midplane.

Without the Hall term, we can take $\chi_z \rightarrow \infty$ to find $dB_x/dB_y \approx -2\Lambda_z$, which is close to zero at the disk interior. Therefore, B_x approaches zero in the highly resistive midplane. This is consistent with the results from run R1b5H0 shown in Figure 1, where B_x is strongly suppressed towards the midplane region.

With the Hall term, since we have $\Lambda_z \ll 1$ and $|\chi_z| \ll 1$ in the disk interior, then $dB_x/dB_y \approx -\Lambda_z/\chi_z$. This indicates that B_x can possess much larger values than the purely resistive case. It is also clear that the sign of dB_x/dB_y should depend on the polarity of magnetic field. However, this is not the case as seen from Figure 1. In both $B_z > 0$ and $B_z < 0$ cases, we always see B_x and B_y have opposite signs within $z \sim 2H$. This indicates that the assumption $v_{Bx} = 0$ is no longer valid.

In Table 1, we show the value of v_{Bx} (or v_{Br} in the table) measured from our simulations. We see that without the Hall term, the value of v_{Bx} is very close to zero in run R1b5H0. With the inclusion of the Hall term, v_{Bx} deviates substantially from 0, and is negative (positive) for $B_z > 0$ ($B_z < 0$). This means that poloidal magnetic flux is transported inward (outward) at some significant velocities ($5\% - 15\%c_s$), much faster than the velocity of the accretion flow. However, we emphasize that value of v_{Bx} should be in principle determined by the global

conditions and can not be controlled in our local simulations. The general properties of the wind solution have been found to depend very weakly on the exact value of v_{Bx} (Wardle & Koenigl 1993). Moreover, the measured values of v_{Bx} are still much less than the sound speed, hence we do not expect the properties of the supersonic wind to be strongly affected. Therefore, the values of v_{Bx} listed in Table 1 should mainly be taken for reference but not to be taken seriously for studying magnetic flux transport.

4.3. General Properties of the New Wind Solutions

As introduced in Section 2.5, we separate the wind solution into a disk zone and a wind zone. They are divided at $z = z_b$, the base of the wind. Conventionally, z_b is defined as the point where the azimuthal velocity transitions from sub-Keplerian to super-Keplerian (Wardle & Koenigl 1993), which is adopted in our previous studies (i.e., $v'_y = 0$ in shearing-box simulations). For our new wind solutions, we find that this location is well defined when $B_z < 0$, as can be seen from the second row of Figure 1, where $|v'_y|$ shows a clear kink in the logarithmic plot at about $z = 4.2H$. This is only slightly smaller than $z_b \approx 4.3H$ in the Hall-free run R1b5H0. When $B_z > 0$, we see that at about the same location, v'_y undergoes a minimum but does not reverse sign. Since other aspects of this solution does not change significantly, to maintain consistency with our Hall-free run R1b5H0, we modify the definition of z_b as follows: moving from disk surface downward, z_b is located at where $|v'_y|$ experiences a minimum for the first time. With this definition, the location of z_b for our run R1b5H+ is exactly at $z \approx 4.3H$, same as the Hall-free case.

Below we discuss the general properties of the new wind solutions, focusing on the transport of mass and angular momentum.

4.3.1. Angular Momentum Transport by Disk Wind

Angular momentum transport by disk wind has been discussed in Section 2.5. With the physical wind symmetry as enforced in our simulations, The wind-driven

accretion rate \dot{M}_V is proportional to the wind stress $T_{z\phi}^{z_b}$, and can be estimated by Equation (16). Their values are provided in Table 1. For our fiducial run ($\beta_0 = 10^5$ at 1AU), the wind-driven accretion rates in both magnetic polarities are well above the desired value of $10^{-8} M_\odot \text{yr}^{-1}$.

We see that including the Hall term, the wind-driven accretion rates is modestly increased (decreased) in the case of $B_z > 0$ ($B_z < 0$) comparing with the Hall-free run R1b5H0. Since $T_{z\phi} \propto -B_y B_z$ with B_z being constant in the disk, the modest increase/reduction is directly related to the amplification/suppression of B_y discussed in Section 4.1.

4.3.2. Radial Transport of Angular Momentum

Besides the vertical extraction of angular momentum via disk wind, angular momentum can also be transported radially outward within the disk, which is characterized by the $R\phi$ component of the stress tensor $T_{R\phi}$

$$T_{R\phi} \equiv T_{R\phi}^{\text{Rey}} + T_{R\phi}^{\text{Max}} = \overline{\rho v_x v_y'} - \frac{1}{4\pi} \overline{B_x B_y}, \quad (24)$$

where the overline represents horizontal average. The Shakura-Sunyaev α is obtained by vertically integrating $T_{R\phi}$ across the disk zone

$$\alpha \equiv \frac{\int_{-z_b}^{z_b} T_{R\phi} dz}{c_s^2 \int \rho dz}. \quad (25)$$

Our results indicate that the Maxwell stress $T_{R\phi}^{\text{Max}}$ is always orders of magnitude larger than the Reynolds stress $T_{R\phi}^{\text{Rey}}$, hence in Table 1 we only show the value of α^{Max} resulting from $T_{R\phi}^{\text{Max}}$ only. Since our solutions are purely laminar, contribution to $T_{R\phi}^{\text{Max}}$ comes from ordered horizontal magnetic field that is winded up to transport angular momentum outward.

Assuming steady state accretion, the accretion rate resulting from radial angular momentum transport then reads

$$\dot{M}_R = \frac{2\pi}{\Omega} \alpha c_s^2 \Sigma \approx 0.82 \times 10^{-8} M_\odot \text{yr}^{-1} \left(\frac{\alpha}{10^{-3}} \right) R_{\text{AU}}^{-1/2}, \quad (26)$$

where subscript ‘R’ represents accretion is driven by radial angular momentum transport, and in the second equation we have adopted the MMSN disk model. The values of α^{Max} and the corresponding \dot{M}_R are also listed in Table 1.

We see that including the Hall term, α^{Max} is substantially enhanced (reduced) in the case of $B_z > 0$ ($B_z < 0$). The main reason again lies in the discussions in Section 4.1. In the case of $B_z > 0$, the enhancement of B_x around the peak of magnetic field strength ($z = 2 - 3H$ in Figure 1) due to the Hall term and the further shear-amplification of B_y both contribute to enhance $T_{R\phi}^{\text{Max}}$. From Table 1 we see that compared with the Hall-free run, α^{Max} is increased by a factor of ~ 8 . In the case of $B_z < 0$, the reduction and reversal of B_x together with reduced B_y naturally leads to much smaller α^{Max} .

The radial transport of angular momentum by the large scale magnetic field was mentioned but not empha-

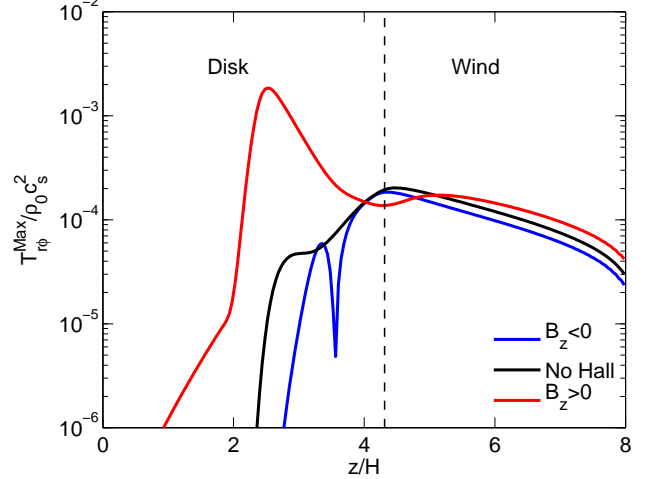


FIG. 3.— The vertical profile of the Maxwell stress $T_{r\phi}^{\text{Max}}$ for our three fiducial simulations R1b5H− (blue), R1b5H0 (black) and R1b5H+ (red). Note that in all cases the sign of $T_{r\phi}^{\text{Max}}$ is positive except the left part of the blue curve. The vertical dashed line marks the location of the base of the wind.

sized in our earlier work of Bai & Stone (2013b), since its contribution is much smaller than that from wind-driven accretion. With the Hall effect and aligned magnetic field, however, the large-scale Maxwell stress already contributes a non-negligible fraction of the angular momentum transport, as read from Table 1, and this term alone is sufficient to account for the typically observed accretion rates in PPDs. On the other hand, for anti-aligned magnetic field geometry, contribution from α^{Max} is rendered completely negligible.

4.3.3. Wind-driven Accretion Flow

In our simulations, the wind stress $T_{z\phi}$ directly corresponds to an inward accretion mass flux, while there is no mass flux associated with radial angular momentum transport due to our shearing-sheet formulation where radial gradients are ignored. Here we focus on the distribution of the wind-driven accretion mass flux.

We see from the second row of Figure 1 that in all three runs R1b5H($\pm, 0$), the radial velocity transitions from being positive near the vertical boundary, to negative somewhere below the base of the wind, which corresponds to the accretion flow. Interestingly, the vertical distribution of the accretion flow is different from the three runs: for $B_z < 0$ the inflow is located at larger vertical height compared with the Hall-free case, while for $B_z > 0$ the inflow is located further towards the disk interior. To characterize the basic properties of such inward mass flux, we identify the maximum inflow velocity $v_{\text{in,max}}$ and the location where it is achieved $z_{\text{in,max}}$, and list their values in Table 1.

We note that the location of the inflow corresponds to where the wind stress $T_{z\phi}$ is exerted to the disk. The reduction in $T_{z\phi}$ (or effectively B_y) towards disk midplane is directly related to the torque per unit length received by the gas hence the rate of the gas inflow. For $B_z > 0$, magnetic field is amplified towards deeper layers, hence the inflow of gas is located closer to the disk midplane; while the contrary applies for the $B_z < 0$ case. This is

TABLE 1
FIDUCIAL RUNS AND VARIATIONS.

| Run | α^{Max} | $\dot{M}_{R,-8}$ | $T_{z\phi}^{z_b}$ | $\dot{M}_{V,-8}$ | \dot{M}_w | $v_{\text{in,max}}$ | $z_{\text{in,max}}$ | v_{Br} | z_b | z_A |
|-------------|-----------------------|------------------|-----------------------|------------------|-----------------------|-----------------------|---------------------|-----------------------|-------|-------|
| R1b5H+ | 1.08×10^{-3} | 0.89 | 1.53×10^{-4} | 6.27 | 2.81×10^{-5} | -0.023 | 2.48 | -0.24 | 4.31 | 5.06 |
| R1b5H0 | 1.23×10^{-4} | 0.10 | 1.19×10^{-4} | 4.87 | 1.65×10^{-5} | -0.012 | 2.56 | -1.0×10^{-3} | 4.31 | 5.98 |
| R1b5H- | 5.25×10^{-5} | 0.043 | 9.75×10^{-5} | 4.00 | 1.19×10^{-5} | -0.072 | 3.48 | 0.074 | 4.27 | 6.40 |
| M03-R1b5H+ | 4.36×10^{-3} | 1.07 | 5.12×10^{-4} | 6.30 | 9.30×10^{-5} | -0.024 | 1.94 | -0.22 | 4.06 | 4.81 |
| M03-R1b5H0 | 4.26×10^{-4} | 0.10 | 3.93×10^{-4} | 4.84 | 5.34×10^{-5} | -0.011 | 2.06 | -7.5×10^{-4} | 4.06 | 5.81 |
| M03-R1b5H- | 1.90×10^{-4} | 0.047 | 3.23×10^{-4} | 3.97 | 3.86×10^{-5} | -0.073 | 3.15 | 0.067 | 4.02 | 6.27 |
| M3-R1b5H+ | 3.11×10^{-4} | 0.77 | 5.10×10^{-5} | 6.27 | 9.48×10^{-6} | -0.022 | 2.90 | -0.25 | 4.52 | 5.23 |
| M3-R1b5H0 | 4.12×10^{-5} | 0.10 | 3.95×10^{-5} | 4.86 | 5.65×10^{-6} | -0.012 | 2.98 | -1.1×10^{-3} | 4.56 | 6.10 |
| M3-R1b5H- | 1.80×10^{-5} | 0.044 | 3.27×10^{-5} | 4.02 | 4.04×10^{-6} | -0.071 | 3.73 | 0.080 | 4.52 | 6.56 |
| nogr-R1b5H+ | 1.05×10^{-2} | 8.62 | 2.42×10^{-4} | 9.94 | 4.63×10^{-5} | -2.1×10^{-3} | 1.19 | -0.28 | 4.06 | 4.98 |
| nogr-R1b5H0 | 2.23×10^{-4} | 0.18 | 1.29×10^{-4} | 5.29 | 1.91×10^{-5} | -7.9×10^{-3} | 2.31 | 6.8×10^{-4} | 4.40 | 5.81 |
| nogr-R1b5H- | 7.67×10^{-5} | 0.063 | 1.11×10^{-4} | 4.57 | 1.47×10^{-5} | -0.048 | 3.27 | 0.022 | 4.27 | 6.10 |
| X29-R1b5H+ | 4.90×10^{-4} | 0.40 | 1.46×10^{-4} | 6.02 | 2.58×10^{-5} | -0.022 | 2.81 | -0.44 | 4.10 | 5.02 |
| X29-R1b5H0 | 1.28×10^{-4} | 0.11 | 1.15×10^{-4} | 4.72 | 1.57×10^{-5} | -0.012 | 2.69 | 0.019 | 4.31 | 6.02 |
| X31-R1b5H+ | 1.84×10^{-3} | 1.51 | 2.43×10^{-4} | 9.97 | 3.19×10^{-5} | -0.026 | 2.27 | -0.075 | 3.73 | 5.31 |
| X31-R1b5H0 | 1.73×10^{-4} | 0.15 | 1.55×10^{-4} | 6.35 | 2.01×10^{-5} | -0.014 | 2.40 | -4.6×10^{-4} | 3.94 | 5.77 |
| X31-R1b5H-* | 7.16×10^{-5} | 0.059 | 1.18×10^{-4} | 4.85 | 1.52×10^{-5} | -0.14 | 3.31 | -1.3×10^{-3} | 4.10 | 6.02 |

See Section 3.2 for description of simulation runs and naming conventions. The last run (with *) is eventually unstable, where values are taken before the instability takes over. The results are mainly discussed in Section 5.1.

List of physical quantities in the Table are, α^{Max} : Shakura-Sunyaev α due to Maxwell stress; $\dot{M}_{R,-8}$: accretion rate due to radial transport of angular momentum ($10^{-8}M_{\odot} \text{ yr}^{-1}$); $T_{z\phi}^{z_b}$: the wind stress (natural unit); $\dot{M}_{V,-8}$: wind-driven accretion rate ($10^{-8}M_{\odot} \text{ yr}^{-1}$); \dot{M}_w : single-sided mass outflow rate (natural unit), $v_{\text{in,max}}$: maximum inflow velocity (c_s); $z_{\text{in,max}}$: location of the maximum inflow velocity (H), v_{Br} : radial drift velocity of vertical magnetic flux; z_b : location of the base of the wind; z_A : location of the Alfvén point.

in line with the interpretation at the end of Section 4.1 that $B_z > 0$ allows the gas deeper towards midplane to be better coupled to the magnetic field.

4.3.4. Disk Outflow

The outflow mass loss rate in the disk wind is not well characterized in shearing-box simulations, and is decreased with increasing the vertical box size, as studied and discussed extensively in Fromang et al. (2013) for turbulent simulations and Bai & Stone (2013b) for the laminar wind case. Here, we are not concerned with the absolute mass loss rate, but focus on the relative dependence of the mass outflow rate on physical quantities such as magnetic polarity (this subsection), β_0 , disk radii (Section 5), where shearing-box should provide more reliable results.

The measured mass loss rate ρv_z from our simulations are listed in Table 1.⁷ We see that with $B_z > 0$ ($B_z < 0$), the wind mass loss rate is increased (reduced) compared with the Hall-free case, consistent with the wind being stronger (weaker) discussed earlier. The increase (reduction) in the outflow mass flux is mainly due to the higher (lower) gas density at the base of the wind, as a result of larger (smaller) magnetic pressure support due to the Hall term. The change in the mass outflow rate is accompanied by the change in the location of the Alfvén point, z_A , which is defined as the location where the vertical velocity equals to the vertical Alfvén velocity $v_z(z_A)^2 = B_z^2/4\pi\rho(z_A)$. As discussed in Bai & Stone (2013b), larger outflow rate corresponds to lower Alfvén point, and vice versa (see their Section 4.5).

⁷ Note that the values reported correspond to single-sided mass loss rate, while the Tables in Bai & Stone (2013b) and Bai (2013) quote the mass loss rate from both sides of the disk.

5. SIMULATION RESULTS: PARAMETER STUDY OF THE WIND SOLUTIONS

In this section, we consider much wider range of parameters and discuss how they affect the properties of the new disk wind solutions. We first consider variations to our fiducial solution at 1AU with $\beta_0 = 10^5$ in Section 5.1, with the list of runs and results shown in Table 1. We then vary the radial location and vertical field strength and discuss the results in Sections 5.2 to 5.4, with the list of runs provided in Table 2.

5.1. Variations to Fiducial Runs

Given our fiducial parameters at $R = 1\text{AU}$ with $\beta_0 = 10^5$, we further performed simulations with different disk mass, grain abundance and X-ray luminosity as listed in Table 1, which help better understand the properties of the wind solutions.

We first vary the disk surface density by a factor of 3 and 0.3 (labeled by “M3” and “M03”). Accordingly, we have also varied the strength of the net vertical magnetic field so that the physical value of the field strength remains the same (hence $\beta_0 = 3 \times 10^5$ and $\beta_0 = 3 \times 10^4$ respectively). Looking from Table 1 we see that the wind-driven accretion rate \dot{M}_V almost remain identical as in the fiducial run under these variations, for both $B_z > -$ and $B_z < 0$. Similarly, the measured wind mass loss rate \dot{M}_w also remain approximately unchanged when converting from numerical to physical units ($\times 0.3$ for M03 runs and $\times 3$ for M3 runs). The results are consistent with the Hall-free case studied in Bai & Stone (2013b), and indicate that the strength of the wind is solely determined by the physical strength of the magnetic field. Also, the rate of radial angular momentum transport is more or less unaffected by the variation of disk surface density.

We also considered a run using grain-free chemistry

TABLE 2
LIST OF SIMULATIONS FOR EXTENDED PARAMETER STUDY.

| Run | α^{Max} | $\dot{M}_{R,-8}$ | $T_{z\phi}^{z_b}$ | $\dot{M}_{V,-8}$ | \dot{M}_w | $v_{\text{in,max}}$ | $z_{\text{in,max}}$ | v_{Br} | z_b | z_A |
|---------|-----------------------|------------------|-----------------------|------------------|-----------------------|-----------------------|---------------------|-----------------------|-------|-------|
| R03b5H+ | 2.71×10^{-4} | 0.41 | 1.00×10^{-4} | 10.1 | 9.89×10^{-6} | -0.072 | 3.27 | -0.36 | 4.06 | 6.19 |
| R03b5H0 | 6.86×10^{-5} | 0.10 | 7.20×10^{-5} | 7.28 | 6.90×10^{-6} | -4.9×10^{-2} | 3.19 | -1.0×10^{-3} | 4.23 | 7.06 |
| R03b5H- | 3.26×10^{-5} | 0.049 | 5.52×10^{-5} | 5.58 | 5.49×10^{-6} | -0.12 | 3.69 | 0.17 | 4.44 | 7.48 |
| R03b6H+ | 1.29×10^{-4} | 0.19 | 1.94×10^{-5} | 1.96 | 4.15×10^{-6} | -0.015 | 3.15 | -0.19 | 4.69 | 5.23 |
| R03b6H0 | 1.39×10^{-5} | 0.021 | 1.48×10^{-5} | 1.49 | 2.33×10^{-6} | -1.3×10^{-2} | 3.35 | -1.7×10^{-3} | 4.69 | 5.98 |
| R1b4H+ | 1.81×10^{-3} | 1.49 | 7.37×10^{-4} | 30.2 | 6.11×10^{-5} | -0.096 | 2.69 | -0.40 | 3.60 | 6.60 |
| R1b4H0 | 6.13×10^{-4} | 0.50 | 5.51×10^{-4} | 22.6 | 4.64×10^{-5} | -0.047 | 2.44 | -3.6×10^{-3} | 3.81 | 7.40 |
| R1b4H- | 3.03×10^{-4} | 0.25 | 4.39×10^{-4} | 18.0 | 3.90×10^{-5} | -0.13 | 3.02 | 0.20 | 3.98 | 7.77 |
| R1b5H+ | 1.08×10^{-3} | 0.89 | 1.53×10^{-4} | 6.27 | 2.81×10^{-5} | -0.023 | 2.48 | -0.24 | 4.31 | 5.06 |
| R1b5H0 | 1.23×10^{-4} | 0.10 | 1.19×10^{-4} | 4.87 | 1.65×10^{-5} | -0.012 | 2.56 | -1.0×10^{-3} | 4.31 | 5.98 |
| R1b5H- | 5.25×10^{-5} | 0.043 | 9.75×10^{-5} | 4.00 | 1.19×10^{-5} | -0.072 | 3.48 | 0.074 | 4.27 | 6.40 |
| R1b6H+ | 3.32×10^{-4} | 0.27 | 3.97×10^{-5} | 1.63 | 1.06×10^{-5} | -4.4×10^{-3} | 2.40 | -0.12 | 4.19 | 4.64 |
| R1b6H0 | 1.77×10^{-5} | 0.015 | 2.57×10^{-5} | 1.05 | 4.81×10^{-6} | -3.1×10^{-3} | 2.73 | -7.4×10^{-4} | 4.40 | 5.44 |
| R3b4H+ | 1.29×10^{-2} | 6.11 | 1.15×10^{-3} | 20.7 | 1.77×10^{-4} | -1.6×10^{-2} | 1.52 | -0.27 | 3.98 | 4.94 |
| R3b4H0 | 1.07×10^{-3} | 0.51 | 9.00×10^{-4} | 16.2 | 1.07×10^{-4} | -8.7×10^{-3} | 1.73 | -2.1×10^{-4} | 3.94 | 6.15 |
| R3b4H- | 5.73×10^{-4} | 0.27 | 7.98×10^{-4} | 14.3 | 8.68×10^{-5} | -0.052 | 2.64 | 0.11 | 3.90 | 6.52 |
| R3b5H+ | 4.79×10^{-3} | 2.27 | 2.89×10^{-4} | 5.21 | 6.79×10^{-5} | -1.8×10^{-3} | 1.40 | -0.093 | 3.85 | 4.39 |
| R3b5H0 | 1.66×10^{-4} | 0.078 | 2.04×10^{-4} | 3.67 | 3.41×10^{-5} | -2.5×10^{-3} | 1.85 | -1.1×10^{-4} | 4.02 | 5.27 |
| R3b6H+ | 1.23×10^{-3} | 0.58 | 7.76×10^{-5} | 1.40 | 2.39×10^{-5} | -4.5×10^{-4} | 1.44 | -0.058 | 3.85 | 4.19 |
| R5b4H+ | 2.06×10^{-2} | 7.54 | 1.52×10^{-3} | 18.6 | 2.68×10^{-4} | -0.017 | 0.23 | -0.099 | 3.81 | 4.56 |
| R5b4H0 | 1.28×10^{-3} | 0.47 | 1.17×10^{-3} | 14.4 | 1.55×10^{-4} | -4.0×10^{-3} | 0.0 | -1.1×10^{-4} | 3.81 | 5.64 |
| R5b4H- | 6.89×10^{-4} | 0.25 | 1.02×10^{-3} | 12.5 | 1.22×10^{-4} | -0.029 | 2.40 | 0.073 | 3.77 | 6.02 |
| R5b5H+ | 6.29×10^{-3} | 2.31 | 3.95×10^{-4} | 4.84 | 1.02×10^{-4} | -5.0×10^{-3} | 0.10 | -0.046 | 3.69 | 4.14 |
| R5b5H0 | 1.86×10^{-4} | 0.068 | 2.54×10^{-4} | 3.11 | 4.50×10^{-5} | -6.9×10^{-4} | 1.52 | -7.2×10^{-5} | 3.90 | 5.06 |
| R5b6H+ | 2.13×10^{-3} | 0.78 | 9.00×10^{-5} | 1.10 | 3.86×10^{-5} | -1.3×10^{-3} | 0.0 | -0.043 | 4.64 | 3.94 |
| R8b4H+ | 1.23×10^{-2} | 3.57 | 1.81×10^{-3} | 15.6 | 3.12×10^{-4} | -0.028 | 0.10 | -6.5×10^{-3} | 3.73 | 4.73 |
| R8b4H0 | 1.84×10^{-3} | 0.53 | 1.52×10^{-3} | 13.1 | 2.20×10^{-4} | -1.1×10^{-2} | 0.0 | 0 | 3.65 | 5.27 |
| R8b5H+ | 3.65×10^{-3} | 1.06 | 4.92×10^{-4} | 4.24 | 1.13×10^{-4} | -7.6×10^{-3} | 0.06 | -3.8×10^{-3} | 3.56 | 4.27 |
| R8b6H+ | 1.16×10^{-3} | 0.34 | 1.37×10^{-4} | 1.18 | 3.74×10^{-5} | -1.9×10^{-3} | 0.0 | -3.7×10^{-3} | 3.52 | 4.10 |
| R15b4H+ | 6.72×10^{-3} | 1.42 | 2.30×10^{-3} | 12.4 | 4.01×10^{-4} | -0.027 | 0.06 | -1.6×10^{-3} | 3.52 | 4.73 |

Same as Table 1, and see Section 3.2 for description of simulation runs and naming conventions. Results are mainly discussed in Section 5.3-5.4.

labeled by “nogr”. We find that the strength of the disk wind, characterized by $T_{z\phi}^{\text{Max}}$ and \dot{M}_w , is typically stronger than the fiducial case for both $B_z > 0$ and $B_z < 0$, though the enhancement is only modest, which is again consistent with findings in Bai & Stone (2013b) for the Hall-free case. However, in the case of $B_z > 0$, the enhancement of α^{Max} is substantial. This is because the reduced magnetic diffusivity towards midplane (by ~ 4 orders of magnitude, see Figure 1 of Bai (2011a)) makes the magnetic field amplification discussed in Section 4.1 extend to much deeper regions than the fiducial case. While the field strength at the wind base remain similar, the deeper penetration with continued amplification that acts to both $|B_x|$ and $|B_y|$ leads to α^{Max} about 10 times larger than the fiducial case. A similar effect will be discussed in Figure 6 in Section 5.3.

Finally, we vary the X-ray luminosity to $L_X = 10^{29}$ and 10^{31} ergs s $^{-1}$ to study the role of X-ray ionization on the wind properties. The range of variation is in accordance with observed scatters of X-ray luminosities in young stars (Preibisch et al. 2005), which also accounts for the fact that X-ray luminosities in young stars are highly variable (Wolk et al. 2005). We find that reducing the X-ray luminosity only modifies the properties of the wind slightly, which is mainly because the wind is launched from the surface layer dominated by FUV ionization. On the other hand, increasing the X-ray lumi-

nosity leads to modest increase of the wind strength by allowing the wind to be launched from deeper regions (due to enhanced ionization, see the values of z_b in Table 1).

Most interestingly, we find that the wind solution becomes unstable for the case with $B_z < 0$ and enhanced X-ray ionization⁸. In Figure 4 we show the time evolution of the horizontal magnetic field in our run X31-R1b5H-. After the inclusion of the Hall term at $t = 480\Omega^{-1}$, while the system quickly relaxes to a new configuration, it then becomes unstable and the horizontal field flips in less than 10 orbits. This flip phenomenon then repeats itself almost periodically. The cause of the flip, as well as the consequences will be discussed in the next subsection in combination with a wider range of runs. Despite being unstable, the bulk of the configuration still consists of a disk wind. The values shown in Table 1 for this run are obtained by measuring the wind properties from $t = 498 - 510$, and we see that in between the magnetic flips, the properties of the disk wind is also modestly enhanced compared with the Hall-free case.

5.2. Stability of the Wind Solutions

⁸ For $L_X = 10^{29}$ with $B_z < 0$, we find similar unstable behavior for more subtle reasons.

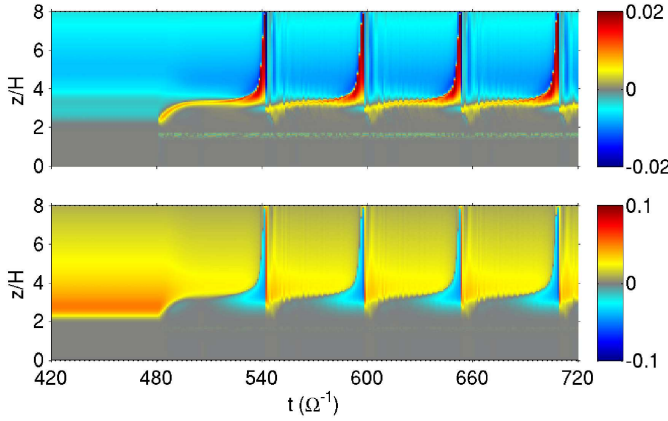


FIG. 4.— Time evolution of the magnetic field profile B_x (upper panels) and B_y (lower panels) around the time the Hall effect is turned on at $t = 480\Omega^{-1}$, for our run X31-R1b5H-, which shows periodic flips of horizontal fields.

We have first repeated our fiducial simulations R1b5H($\pm, 0$) discussed in the previous section with a full 3D box with horizontal box size enlarged to $4H \times 8H$ resolved by 96×96 cells. From this test we verify that the new wind solutions are stable in 3D. This is reassuring since in the presence of AD with large-scale toroidal field, most unstable MRI modes may have non-zero radial wave numbers (Kunz & Balbus 2004; Desch 2004; Pandey & Wardle 2012), which can not be captured in our quasi-1D simulations.

On the other hand, a number of runs in our quasi-1D simulations never relax to a steady state. Instead, they show similar behaviors as our run X31-R0b5- with the large-scale horizontal field changing sign quasi-periodically. Whenever this happens, steady state wind solution is unlikely possible, and we no longer show the run results in Table 2.

In Figure 5 we show the stability map for all the quasi-1D simulations we performed in the parameter exploration of R_{AU} and β_0 . Compared with the Hall-free situation studied in Bai (2013) (see his Figure 7), it is clear that when $B_z > 0$, the parameter space for stability is considerably enlarged: stable solutions can be found with weaker vertical field and outer disk radii; while if $B_z < 0$, the parameter space for stability is largely reduced: stable solutions can only be found with stronger vertical field and at smaller disk radii.

The onset of the instability for the unstable runs is due to the MRI, and the observed stability trend can be readily understood from the Hall-MRI linear dispersion relation.

As discussed in Section 2.4, the main reason for the existence of stable (Hall-free) wind solutions is that the MRI is suppressed in the midplane due to excessively large resistivity, while in the surface layer the AD-modified unstable wavelength is too large to be fitted into the disk. In the inner disk ($\lesssim 10$ AU), the midplane region is always too resistive. The MRI can take place in the surface layer only for extremely weak vertical field ($\beta_0 \gtrsim 10^6$) which brings down the unstable MRI wavelength for the MRI to develop properly.

The main role played by the Hall effect is that, for $B_z > 0$, the unstable MRI modes shift to smaller $k_z v_{Az}$,

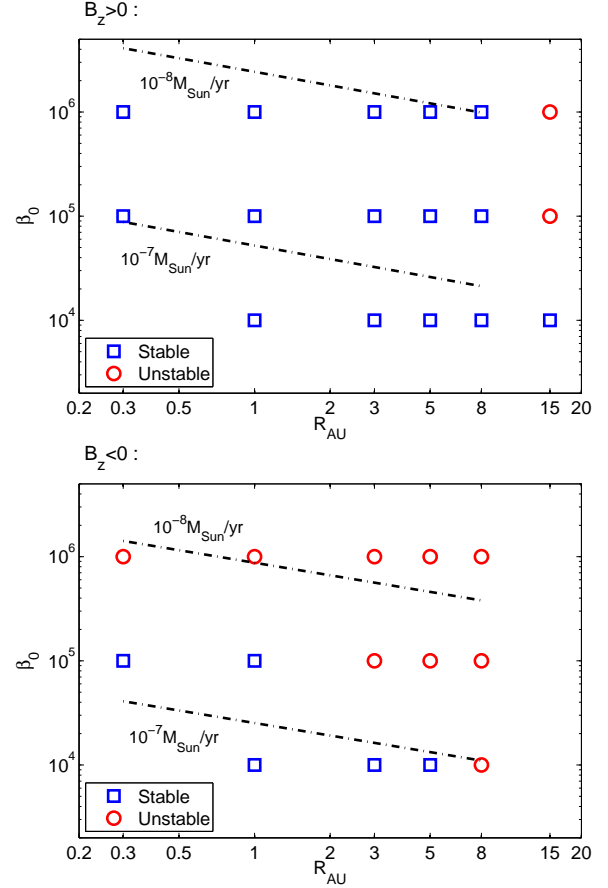


FIG. 5.— The stability of the wind solution in parameter space of R_{AU} and β_0 (see Equation 14), with other parameters being fiducial. Upper and lower panels are for $B_z > 0$ and $B_z < 0$ respectively. Stable regions are marked with blue squares, while unstable regions are marked by red circles, which in reality may lead to weak turbulence. The two dashed lines indicate the desired β_0 as a function of radius for the wind-driven accretion rate to be 10^{-8} and $10^{-7} M_{\odot} \text{ yr}^{-1}$, based on the fitting formulas (28) and (30) in Section 5.4.

corresponding to longer wavelength for fixed vertical field (Wardle 1999, and see Figure 9 in the Appendix). Therefore, to make the system unstable, further weaker vertical field (smaller v_{Az}) is required. This explains why for $B_z > 0$ the parameter space for stability is enlarged.

For $B_z < 0$ (hence $\chi < 0$), unstable MRI modes exist only for $|\chi| > 1/2$. Without dissipation, the unstable modes essentially extends to infinitely small scales for $1/2 < |\chi| < 5/4$ (Wardle 1999). With dissipation, mostly ambipolar diffusion, the unstable modes cutoff at finite wavelength, yet still extend to scales smaller than the Hall-free case to activate the MRI. This can again be seen from Figure 9 in the Appendix⁹. Since $|\chi|$ transitions from $\ll 1$ to $\gg 1$ from midplane to surface, it always falls in this range above certain height in the disk. At this location, the unstable MRI modes extend to larger $k_z v_{Az}$, corresponding to shorter wavelength for fixed vertical field, making it more suscepti-

⁹ Since the MRI dispersion relation in the presence of pure vertical field is identical for the case with Ohmic resistivity and AD (Wardle 1999), one can simply replace Λ by Λm in that figure to see the trend.

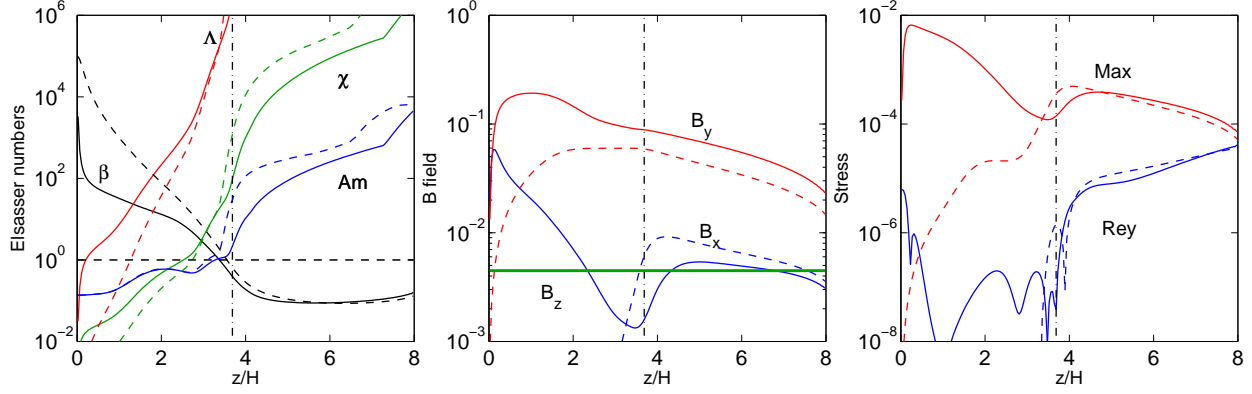


FIG. 6.— The vertical profile of the Elsasser numbers (left), the three magnetic field components (middle) and the $R\phi$ components of Maxwell and Reynolds stress (right) for our runs R5b5H+ (solid) and R5b5H0 (dashed). The vertical dash-dotted line indicate the location of the wind base for run R5b5H+.

ble to the MRI. Indeed, when checking with Figure 4 as well as many other unstable runs, we find that regions that first lead to instability (at $z \sim 3 - 3.5$ in Figure 4) are typically associated with $|\chi|$ transition through order unity.

The above discussions are also consistent with the analysis of the MRI linear modes presented by Wardle & Salmeron (2012).

Connecting to the discussions at the end of the previous section, we note that the range of stability can depend on other parameters such as grain abundance and X-ray ionization. It is conceivable that, for example, with enhanced X-ray ionization and reduced grain abundance, the range of radii where the laminar wind solution holds would shrink, at least in the case of $B_z < 0$.

5.3. Solutions towards Outer Radii

Towards the outer disk radii, external ionization penetrates deeper towards disk midplane. Together with the reduced gas density, this leads to rapid increase of the ionization fraction, which makes the region around disk midplane better coupled with magnetic field. Two consequences result. First, the wind is launched from a lower height compared with our fiducial runs, leading to higher mass outflow rate and wind stress (in code units). This has been discussed in Bai (2013). Second, in the presence of the Hall effect, this makes magnetic field enhancement more prominent in the case of $B_z > 0$.

In Figure 6, we show the profiles of the Elsasser numbers, the three magnetic field components, and the $R\phi$ stresses from our runs R5b5H0 and R5b5H+. We see that without the Hall term, the radial field B_x rapidly diminishes towards disk midplane, while with the inclusion of the Hall term, B_x continues to increase towards midplane until it catches up with the toroidal field B_y before diminishing to zero at the midplane enforced by symmetry. The strongly enhanced B_x combined with B_y produce the Maxwell stress α^{Max} that is more than 30 times larger than the Hall-free case. This example is the exaggerated version of the 1AU fiducial runs discussed in detail in Section 4.1. It is similar to the grain-free run discussed in Section 5.1, and also generically applies to other wind solutions at comparable or larger radii listed in Table 2. We also note that at radius $R \geq 5$ AU, the location of maximum inflow velocity $z_{\text{in,max}}$ is generally

either very close or exactly at the disk midplane, indicating that entire disk is actively coupled with magnetic field.

Despite the stronger magnetic activities in the midplane region, the properties of the wind seem to be less affected, as we see that to the right of the vertical dash-dotted line in Figure 6, the magnetic profile, as well as the Maxwell and Reynolds stresses behave in a way very similar to the 1 AU case.

5.4. Angular Momentum Transport and Mass Outflow

In this subsection, we follow the approach of Bai (2013) and study the dependence of the rate of wind-driven angular momentum on R_{AU} and β_0 . Using all the data from Table 2, we fit the wind mass loss rate \dot{M}_w and the wind stress $T_{z\phi}^{z_b}$ in the form of $C R_{\text{AU}}^q \beta_0^{-b}$, where C , q and b are constants.

For $B_z > 0$, there are a total of 15 data points, we find

$$\frac{\dot{M}_w}{\rho_0 c_s} \approx 2.67 \times 10^{-5} \left(\frac{\Sigma_{\text{MMSN}}}{\Sigma} \right) \left(\frac{R}{\text{AU}} \right)^{0.72} \left(\frac{\beta_0}{10^5} \right)^{-0.42}, \quad (27)$$

$$\frac{T_{z\phi}^{z_b}}{\rho_0 c_s^2} \approx 1.65 \times 10^{-4} \left(\frac{\Sigma_{\text{MMSN}}}{\Sigma} \right) \left(\frac{R}{\text{AU}} \right)^{0.51} \left(\frac{\beta_0}{10^5} \right)^{-0.60}. \quad (28)$$

For $B_z < 0$, there are only 5 data points, which still yield a good fit:

$$\frac{\dot{M}_w}{\rho_0 c_s} \approx 1.59 \times 10^{-5} \left(\frac{\Sigma_{\text{MMSN}}}{\Sigma} \right) \left(\frac{R}{\text{AU}} \right)^{0.69} \left(\frac{\beta_0}{10^5} \right)^{-0.50}, \quad (29)$$

$$\frac{T_{z\phi}^{z_b}}{\rho_0 c_s^2} \approx 9.96 \times 10^{-5} \left(\frac{\Sigma_{\text{MMSN}}}{\Sigma} \right) \left(\frac{R}{\text{AU}} \right)^{0.51} \left(\frac{\beta_0}{10^5} \right)^{-0.65}. \quad (30)$$

Without the Hall term, the fitting results are very close to Equations (9) and (10) of Bai (2013) hence we do not repeat. Also note that we quote single-sided mass loss rate while Bai (2013) used mass loss rate from both sides.

In Figures 7, we show the values of the wind mass loss rate and the wind stress from all runs in Table 2 together with the above formulas. We see that these formulas

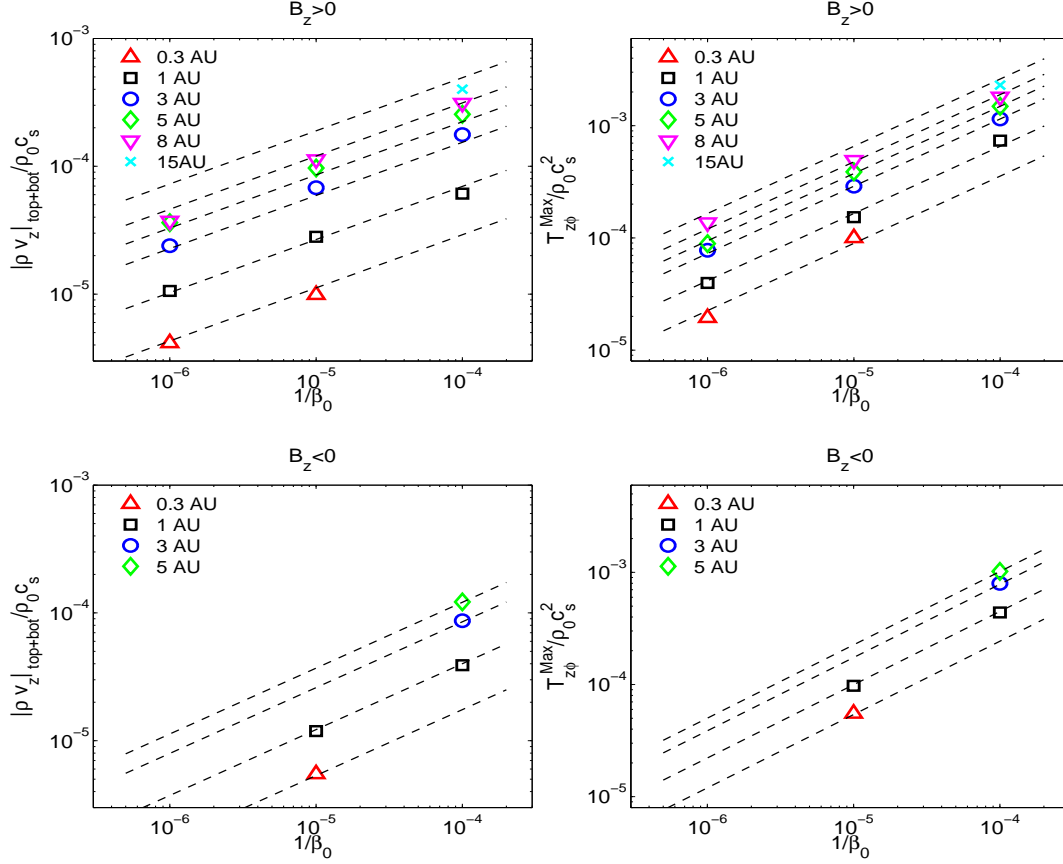


FIG. 7.— Single-sided wind mass loss rate \dot{M}_w (left) and the wind stress $T_{z\phi}^{\text{Max}}$ (right) from all simulations listed in Table 2. Upper and lower panels are for simulations with $B_z > 0$ and $B_z < 0$ respectively. Also plotted in dashed lines are the fitting formulas (27)-(30) applied to appropriate panels with individual lines corresponding to individual radius.

generally fit the data very well. The power law indices of the scaling relations are similar indicating similar wind physics. We have also checked the scalability of α^{Max} and find that while it has the trend to monotonically increases with increasing magnetic flux, the dependence on R_{AU} is not monotonic.

Interpretation of these fitting formula follows from the discussions in Section 3.2 of Bai (2013). With proper unit conversion, i.e., Equation (16), the wind stress $T_{z\phi}^{\text{Max}}$ should provide reliable estimate of the wind-driven accretion rate. When applied to disks with surface densities Σ , one should interpret β_0 as the ratio of the midplane gas pressure of a MMSN disk to the magnetic pressure of the net vertical field. The wind mass loss rate \dot{M}_w , on the other hand, is not well determined in the shearing-box framework (Fromang et al. 2013; Bai & Stone 2013b). The power-law indices in the \dot{M}_w fitting formulas are likely reliable, but the normalizations are likely a significant overestimate.

Using these fitting formulas and Equation (16) assuming MMSN disk, we further show in Figure 5 in dash-dotted lines the desired value of β_0 as a function of R_{AU} for the disk to maintain wind-driven accretion rate of 10^{-8} and $10^{-7} M_{\odot} \text{ yr}^{-1}$. We see that given the typical accretion rate of $10^{-8} - 10^{-7} M_{\odot} \text{ yr}^{-1}$, stable wind solutions for disks with $B_z > 0$ extend up to ~ 15 AU, while for disks with $B_z < 0$, stable solution exists only

up to 3-5 AU. Reducing the accretion rate would lead to reduced radial range of stability.

Based on the fact that the wind-driven accretion rate depends only on the physical strength of the net vertical magnetic field B_{z0} , we can further write down the wind-driven accretion rate in terms of physical field strength as follows

$$\dot{M}_V = 0.82 \times 10^{-8} M_{\odot} \text{ yr}^{-1} R_{\text{AU}}^{1.71} \left(\frac{B_{z0}}{10 \text{ mG}} \right)^{1.2} \quad (31)$$

for the case with $B_z > 0$, and

$$\dot{M}_V = 0.42 \times 10^{-8} M_{\odot} \text{ yr}^{-1} R_{\text{AU}}^{1.87} \left(\frac{B_{z0}}{10 \text{ mG}} \right)^{1.3} \quad (32)$$

for the case with $B_z < 0$. These expressions can be considered as disk-model independent, as long as stable laminar-wind solution exists. The only MMSN scaling comes from the temperature profile, which is reasonable for irradiated disks.

The above formulas are to be compared with the Hall-free formula based on the results of Bai (2013)¹⁰

$$\dot{M}_V = 0.47 \times 10^{-8} M_{\odot} \text{ yr}^{-1} R_{\text{AU}}^{1.90} \left(\frac{B_{z0}}{10 \text{ mG}} \right)^{1.32} \quad (33)$$

¹⁰ We regret the miscalculation in Equation (11) of Bai (2013).

These formulas again capsule the role of the Hall term on the properties of the laminar wind solutions. With similar scalings, they reveal the enhancement and reduction on the strength of disk wind introduced by the Hall term when $B_z > 0$ or $B_z < 0$.

Our results indicate that 10–100mG net vertical magnetic field is necessary to achieve wind-driven accretion rate of $10^{-8} - 10^{-7} M_\odot \text{ yr}^{-1}$ at 1 AU. Stronger field is required for the $B_z < 0$ case and weaker field for $B_z > 0$. For steady-state accretion, the radial profile of B_{z0} should satisfy $B_{z0} \propto R^{-1.43}$ for both magnetic polarities, corresponding to magnetic flux distribution of $\Phi(R) \propto R^{0.57}$, where $\Phi(R)$ denotes the total magnetic flux contained within radius R .

6. SUMMARY AND DISCUSSION

6.1. Summary

In this work, we have successfully implemented the Hall term in the ATHENA MHD code, which enables us to extend our previous study on the gas dynamics of protoplanetary disks (PPDs) to include all three non-ideal MHD effects in a self-consistent manner in local shearing-box simulations. All our simulations include an external vertical magnetic field B_z , which has been realized to be essential (see discussions in Section 2.4). We focus on the inner region of PPDs (up to $\sim 10 - 15$ AU) in this paper where the disk is expected to be largely laminar with accretion driven by a magnetocentrifugal wind.

Our first important finding is that with the inclusion of the Hall term, the conclusion from our previous work (Bai & Stone 2013b; Bai 2013 where only Ohmic resistivity and ambipolar diffusion were included) that the inner disk is largely laminar still holds, with accretion mainly driven by magnetocentrifugal wind. On the other hand, the wind solution is further controlled by the Hall effect in a way that depends on the polarity of the external vertical field (sign of B_z), and we summarize as follows.

For external field being aligned with disk rotation ($B_z > 0$), we find

- The horizontal magnetic field is amplified compared with the Hall-free solutions, leading to stronger magnetocentrifugal disk wind and more efficient (vertical) angular momentum transport by up to $\sim 50\%$.
- The enhanced horizontal magnetic field drives radial transport of angular momentum via large-scale Maxwell stress, which accounts for a considerable fraction of the wind-driven accretion rate.
- The parameter space where a stable laminar wind solution can be found is extended. For typical accretion rate of $10^{-8} - 10^{-7} M_\odot \text{ yr}^{-1}$, radial range of stability extends to ~ 15 AU before the MRI sets in.

For external field being anti-aligned with disk rotation ($B_z < 0$), we find

- The horizontal magnetic field is reduced compared with the Hall-free solutions, leading to weaker disk wind and less efficient (vertical) angular momentum transport by $\sim 20\%$.

- Radial transport of angular momentum by large-scale Maxwell stress is negligible.
- The parameter space for a stable laminar wind solution is substantially reduced. For typical accretion rate of $10^{-8} - 10^{-7} M_\odot \text{ yr}^{-1}$, radial range of stability extends only to $\sim 3 - 5$ AU before the MRI sets in.

The physics behind these differences in opposite magnetic polarities are related to the special properties of the Hall term and the stability properties of the Hall MRI, which are explained in detail in the main text.

All of our simulations cover half of the disk assuming reflection symmetry about disk midplane, as is the convention for constructing disk wind solutions. The magnetocentrifugal wind drives a radial inflow in the disk, whose location is typically not at disk midplane due to excessively large resistivity. With the Hall term, we find that the location for the bulk of the inflow is shifted to higher vertical height with faster velocity for the anti-aligned case ($B_z < 0$), and to lower height with smaller velocity for the aligned case ($B_z > 0$) respectively. This reflects the fact that the Hall term enhances the magnetic coupling between gas and magnetic fields for $B_z > 0$, to allow the inflow to reside deeper, and vice versa.

For our fiducial simulation parameters (1AU with $\beta_0 = 10^5$), we explored the dependence of the wind solution on disk surface density, X-ray ionization and grain abundance. Our results indicate that the properties of the wind solution is largely determined by the physical strength of the vertical magnetic field independent of disk surface density. Enhanced X-ray ionization and reduced grain abundance makes the wind stronger, and may also reduce the radial range of stability for the laminar wind solutions for the $B_z < 0$ case.

Using the MMSN disk model, and using the standard prescriptions of ionization and chemistry, we further explored the dependence of the wind properties on disk radii and the strength of the vertical magnetic field. In the $B_z > 0$ case, magnetic field amplification by the Hall term extends to the midplane for $R \gtrsim 5$ AU (with 10^{-4} of $0.1\mu\text{m}$ grains), which substantially enhances angular momentum transport by large-scale Maxwell stress. The same phenomenon is observed in the grain-free case at 1 AU. The properties of the laminar wind from all our simulations can be well summarized in the fitting formulas (27) to (30). We also provide the disk model independent formulas on the wind-driven accretion rate in Equations (31) and (32). Our results indicate 10–100mG net vertical magnetic field at 1 AU is required to account for typical PPD accretion rates. At fixed accretion rate, stronger (by a factor of ~ 2) net field is needed for $B_z < 0$.

6.2. Discussions

Our work strengthens the notion that the evolution of PPDs is largely governed by the distribution and transport of external poloidal magnetic flux, as suggested in our previous works (Bai & Stone 2013b; Bai 2013). Such large-scale is expected as a natural consequence of star formation: molecular clouds and star-forming cores are all strongly magnetized (e.g., see Crutcher 2012 for a review). Recent dust polarization observations further

reveal the presence of large-scale field threading protostellar cores (Hull et al. 2014), and the large-scale fields appear to be randomly oriented with respect to the direction of protostellar outflows. Considering the Hall effect, the bifurcation of disk wind properties with different polarities of the external magnetic field further suggests that PPDs may evolve differently with different initial magnetic field polarities, and systems with $\mathbf{B} \cdot \boldsymbol{\Omega} > 0$ may achieve higher accretion rate, or retain less magnetic flux (in a self-organized way to avoid accreting too fast) compared with systems with $\mathbf{B} \cdot \boldsymbol{\Omega} < 0$.

On the other hand, the desired level of magnetic flux threading PPDs (at least in the Class II phase) is tiny compared with the amount of magnetic flux threading star-forming cores. Consequently, the process of star formation must also be accompanied by the removal of magnetic flux, which is another major problem in the theory of star formation. It appears that substantial magnetic flux must be removed in order to form the PPD itself to avoid the “magnetic braking catastrophe” (Mellon & Li 2008), which may be achieved via misaligned magnetic field (Hennebelle & Ciardi 2009; Joos et al. 2012), external turbulence (Santos-Lima et al. 2012; Seifried et al. 2012) or non-ideal MHD effects (Li et al. 2011; Krasnopolsky et al. 2011; Tomida et al. 2013). After disk formation, the transport of magnetic flux must be achieved within the disk itself, yet the problem is intrinsically global, and must depend on the overall magnetic field geometry and internal dissipation in the disk (e.g. Lubow et al. 1994). Recently, there have been substantial semi-analytical effort to study magnetic flux transport in thin accretion disks which have revealed complex dependence on the internal disk microphysics (e.g., Guilet & Ogilvie 2012, 2013; Okuzumi et al. 2013; Takeuchi & Okuzumi 2013). Nevertheless, a still missing important ingredient is the launching of magnetic outflow, and it appears that global simulations of PPDs with resolved disk microphysics and sufficiently large vertical domain to accommodate disk outflow is essential towards a better understanding of the problem.

While our results suggest the inner region of PPDs is largely laminar in terms of magnetic activities, it does not exclude the possibility for pure hydrodynamic mechanisms to generate turbulence. In fact, some level of turbulence is probably needed to keep at least some small dust suspended in the disk so as to explain the scattered starlight as well as the near infrared spectral energy distribution (e.g., Stapelfeldt et al. 2003; D’Alessio et al. 2006). Promising candidates of hydrodynamic turbulence may include the Goldreich-Schubert-

Fricke instability (Urpin 2003; Nelson et al. 2013) and the baroclinic vortex amplification (Petersen et al. 2007; Lesur & Papaloizou 2010; Raettig et al. 2013). We note that the survival of both instabilities requires the non-existence of MRI (e.g., Lyra & Klahr 2011), hence the inner disk is probably the most likely region for them to develop, provided that appropriate thermodynamic requirements are met.

A largely laminar inner disk is favorable to many processes of planet formation, including grain growth, planetesimal formation and further growth towards planetary embryos, which were discussed in Bai & Stone (2013b). With the formation of planetary cores, a largely-laminar disk may further alleviate the problem of type-I migration by allowing low-mass planet to open gaps (Goodman & Rafikov 2001; Dong et al. 2011), which may substantially reduce the rate of inward migration. The fact that disks threaded by external magnetic field of different polarities show different stability properties to the MRI might indicate that planet formation and retention is easier for aligned magnetic field geometry because of larger radial extent of the laminar region.

While our simulations have captured the most essential non-ideal MHD physics in the inner region of PPDs, there are still several unresolved problems due to limitations of the shearing-box framework. As discussed in our previous works, important issues include the large-scale kinematics of the wind launched from the disk, the stability of the strong-current layer which carries the wind-driven accretion flow, and the direction of magnetic flux transport. The next step forward would be to address these issues with global simulations, which are planned as our future work; while in the companion paper, we again take the advantage of the shearing-box for its resolving power of disk microphysics and study the Hall-controlled gas dynamics in the outer PPDs.

I am grateful to Jim Stone for helpful discussions on the Hall algorithm at the beginning of the project. I thank H. Nomura for helpful discussions on the FUV ionization/chemistry at disk surface and together with C. Walsh for providing their calculation data. This work is supported for program number HST-HF-51301.01-A provided by NASA through a Hubble Fellowship grant from the Space Telescope Science Institute awarded to XN.B, which is operated by the Association of Universities for Research in Astronomy, Incorporated, under NASA contract NAS5-26555.

APPENDIX

IMPLEMENTATION OF THE HALL TERM IN THE ATHENA MHD CODE

The non-dissipative nature of the Hall term makes the implementation of this term not as straightforward as Ohmic resistivity and ambipolar diffusion. Simple von-Neumann analysis shows that first-order Euler method is unconditionally unstable. Here we consider the alternative scheme suggested by O’Sullivan & Downes (2006, 2007), who showed that dimensionally split method makes a stable Hall-MHD algorithm.

For simplicity, we consider the one-dimensional algorithm. We assume the background magnetic field B_0 is along the x -axis, and consider magnetic field evolution (induction equation) due to the Hall term. The evolutionary equations

read

$$\begin{aligned}\frac{\partial B_y}{\partial t} &= Q_H B_0 \frac{\partial^2}{\partial x^2} B_z, \\ \frac{\partial B_z}{\partial t} &= -Q_H B_0 \frac{\partial^2}{\partial x^2} B_y,\end{aligned}\tag{A1}$$

where $Q_H = \eta_H/B_0$ is the coefficient for the Hall term. To update the magnetic field from step (n) to $(n+1)$, we first update $B_y^{(n)}$ to $B_y^{(n+1)}$ using $B_z^{(n)}$, and then update $B_z^{(n)}$ to $B_z^{(n+1)}$ using $B_y^{(n+1)}$. To show that this method is numerical stable, we perform von-Neumann analysis and decompose magnetic perturbations into Fourier modes. Picking up an arbitrary mode, and assuming $B_y = A_2 \exp(i\omega t) \exp(-ikx)$ and $B_z = A_3 \exp(i\omega t) \exp(-ikx)$, we obtain

$$\begin{aligned}A_2[\exp(i\omega\Delta t) - 1] &= A_3 D_H [2 \cos(k\Delta x) - 2], \\ A_3[\exp(i\omega\Delta t) - 1] &= -A_2 \exp(i\omega\Delta t) D_H [2 \cos(k\Delta x) - 2],\end{aligned}\tag{A2}$$

where Δx and Δt represent grid spacing and timestep, and $D_H \equiv Q_H B_0 \Delta t / \Delta x^2$. Non-trivial solutions demand $A_2 = \pm i A_3 \exp(-i\omega\Delta t/2)$, and

$$\sin \frac{\omega\Delta t}{2} = \pm 2 D_H \sin^2 \frac{k\Delta x}{2}.\tag{A3}$$

We see that for any given k , ω is a real number provided that $2|D_H| \leq 1$, hence the amplitude of the wave is preserved without damping or amplification. The stability constraint is thus given by $|D_H| < 1/2$, or

$$\Delta t_{\text{Hall},0} \leq \frac{\Delta x^2}{2|\eta_H|}.\tag{A4}$$

Using this method, the Hall MHD term is implemented to ATHENA in a operator-split manner. Since ATHENA uses the standard constrained transport (CT) to preserve the divergence free condition, the actual procedure in our implementation follows the same spirit of dimensionally-split update, with the split acting on the Hall electric field $\mathbf{E}^H = Q_H \mathbf{J} \times \mathbf{B}$. We first calculate E_x^H using the original magnetic field. Using E_x^H alone, we update B_y and B_z for a full timestep, from which we calculate E_y^H using the original B_x and updated B_y and B_z . Using E_y^H alone, we further update B_x and B_z for a full timestep. Finally, using the updated field components, we evaluate E_z^H . The obtained Hall electric fields are then combined with the electric fields from Ohmic and AD terms to update the magnetic field via CT.

With shearing-box, we also remap of J_y at radial (shearing-box) boundaries so that the line integral of J_y along the azimuthal direction in the inner and outer radial boundaries are equal. This is necessary to avoid numerical instabilities at radial boundaries, which we have found earlier in the case with the ambipolar diffusion term (Simon et al. 2013b), as well as the Hall term in the context of plasma simulations (Kunz et al. 2014).

In multi-dimensions, the stability criterion becomes more stringent, and also depends on the details of the implementation, which is particularly complicated by the CT algorithm required in the ATHENA MHD code. Using the test problems described in the next Appendix, the following stability criterion is found to be robust

$$\Delta t_{\text{Hall},1} \leq \frac{\Delta x^2}{2d|\eta_H|},\tag{A5}$$

where $d = 1, 2, 3$ represents the dimension of the problem. This is the analog of the stability criterion of a pure diffusion problem (e.g., Ohmic resistivity η_O), where the timestep constraint is $\Delta t \leq \Delta x^2 / 4d\eta_O$.

Finally, we discuss the timestepping in the presence of all three non-ideal MHD terms, which are all implemented in an operator-split manner. The Ohmic and AD terms are parabolic in nature and can be treated jointly as magnetic diffusion with total diffusivity $\eta_{\text{tot}} = \eta_O + \eta_A$, which gives the diffusion timestep constraint $\Delta t_{\text{diff}} < \Delta x^2 / 4d\eta_{\text{tot}}$. The small timestep constraint can be relaxed by applying the super-timestepping (STS) technique (Alexiades et al. 1996), where one employs multiple sub-steps with decreasing size within a super timestep. The initial length of the sub-steps can be significantly larger than the stability constraint Δt_{diff} , but it is later stabilized by progressively small sub-step lengths. This technique has been shown to be very successful in accelerating the calculations with AD (O'Sullivan & Downes 2006, 2007; Choi et al. 2009), and has been implemented and effectively used in our previous works (Bai 2012; Simon et al. 2013b; Bai & Stone 2013b; Bai 2013; Simon et al. 2013a).

Due to the hyperbolic nature of the Hall term, the STS technique can not be used to accelerate the calculation. However, we can still use STS to accelerate the calculation for Ohmic resistivity and AD terms. The overall MHD timestep Δt_{all} is determined by the minimum of the normal MHD timestep Δt_{MHD} (given by the Courant-Friedrichs-Lewy condition) and $\Delta t_{\text{Hall},1}$ (A5), and the diffusion timestep is given by Δt_{diff} . However, we find that the in the presence of strong diffusion, the Hall timestep can be relaxed towards the 1D criterion $\Delta t_{\text{Hall},0}$ (A4). Empirically, we adopt the full MHD timestep to be

$$\Delta t_{\text{all}} = \text{MIN} \left\{ \Delta t_{\text{MHD}}, \text{MIN} \left[\Delta t_{\text{Hall},1} + (\Delta t_{\text{Hall},0} - \Delta t_{\text{Hall},1}) \frac{\eta_{\text{tot}}}{\eta_H}, \Delta t_{\text{Hall},0} \right] \right\}.\tag{A6}$$

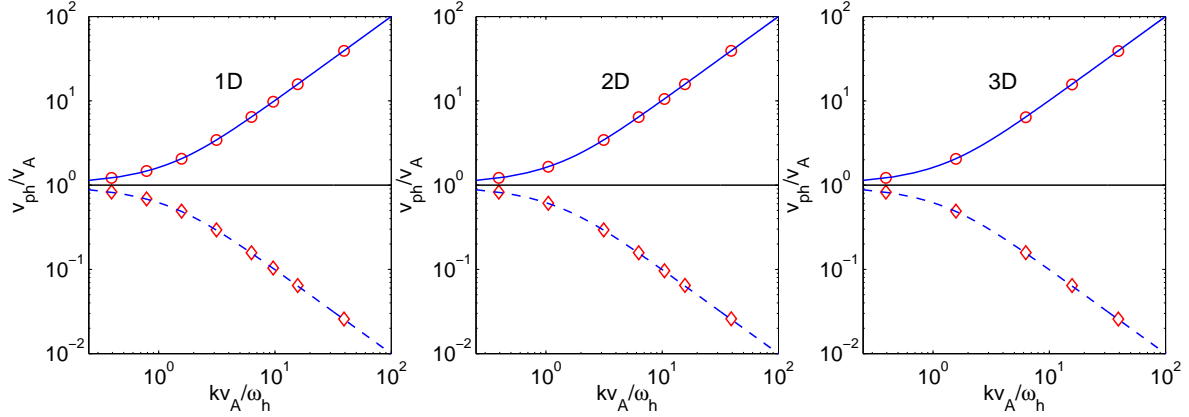


FIG. 8.— The measured dispersion relation for circularly polarized Alfvén waves in 1D (left), 2D (middle) and 3D (right) grids. Upper panels show the results for right handed (whistler) waves, where red circles mark the measured phase velocity $v_{ph} = \omega/k$ normalized by v_A at various wave numbers k (normalized by $\omega_H/v_A = 1/l_H$), and solid blue line indicated the theoretical relation. Lower panels are for left handed waves, with red diamonds and blue dashed lines mark the measured and theoretical dispersion relations respectively. For Ohmic and AD terms, we use STS when $\Delta t_{diff} < \Delta t_{all}$, with details the same as described in Appendix B.3.1 of Bai (2012, PhD thesis), repeated in Appendix A of our later publication (Simon et al. 2013b).

CODE TESTS

We describe two sensitive test problems to demonstrate the successful implementation of the Hall term in ATHENA, where the first problem is reproduced from Appendix B.4.3 of Bai (2012, PhD thesis).

Circularly Polarized Alfvén Wave Test

In the presence of the Hall effect, left and right polarized Alfvén waves propagate at different velocities, which makes it an excellent code test problem. Consider a uniform medium with density ρ_0 and electron density n_e , embedded in a uniform magnetic field \mathbf{B}_0 . For Alfvén mode propagating along \mathbf{B}_0 , the dispersion relation reads

$$\omega^2 - k^2 v_{Az}^2 = \pm \omega k^2 \frac{c B_0}{4\pi n_e e}, \quad (\text{B1})$$

where the plus (minus) sign corresponds to right (left) hand polarizations. The above dispersion relation can be rewritten into a more intuitive form as

$$\omega^2 = \left(1 \pm \frac{\omega}{\omega_H}\right) k^2 v_A^2, \quad (\text{B2})$$

where ω_H is the Hall frequency defined in Equation (10), and it has the clear meaning of being the cut-off frequency for left-handed waves. The right polarized wave is also known as whistler wave and has the asymptotic dispersion property of $\omega \propto k^2$ (for $\omega \gg \omega_H$). Normalizing the wave number by $x \equiv kv_A/\omega_H = kl_H$, the phase velocity is given by

$$\frac{v_{ph}}{v_A} = \frac{\sqrt{x^2 + 4} \pm x}{2}, \quad (\text{B3})$$

where again the plus/minus sign corresponds to right/left polarized Alfvén waves.

We test the linear dispersion relation (B3) by initializing the exact wave eigenvector in a periodic box in 1D, 2D and 3D, with wave amplitude $|\delta \mathbf{B}| = 10^{-4} |\mathbf{B}|$. In 1D, the wave is grid-aligned with wavelength of 1 resolved by 32 cells. In 2D and 3D tests, the wave vectors are not aligned with the grid, and we properly choose box sizes so that the wavelength is also 1: In 2D, the box size is $(\sqrt{5}, \sqrt{5}/2)$ resolved by 64×32 cells and in 3D, the box size is $(3, 1.5, 1.5)$ resolved by $64 \times 32 \times 32$ cells. In Figure 8, we show the measured dispersion relation for right (whistler) and left handed Alfvén waves and compare them with analytical relations. We see that the agreement is excellent in all cases. In particular, we are able to resolve the whistler wave branch up to very large k .

Linear Growth Rate of the Magnetorotational Instability

The second problem aims at testing the coupling between the Hall term and rotation/shear in the context of shearing-box simulations. The test problem is adopted from Sano & Stone (2002a), where we compare the numerical dispersion relation of the MRI with predictions from linear theory. We set up a 3D unstratified shearing-box (cf. Section 2.2 but ignore vertical gravity) threaded by a weak net vertical magnetic field B_0 corresponding to plasma $\beta_0 = 800$. For this test problem, we include both Ohmic resistivity and the Hall term, and consider axisymmetric perturbations of the form $\propto \exp(ikz + \sigma t)$. The linear dispersion then reads (Wardle 1999; Balbus & Terquem 2001)

$$\sigma^4 + \frac{2k^2}{\Lambda} \sigma^3 + \mathcal{E}_2 \sigma^2 + \frac{2k^2}{\Lambda} (k^2 + 1) \sigma + \mathcal{E}_0 = 0, \quad (\text{B4})$$

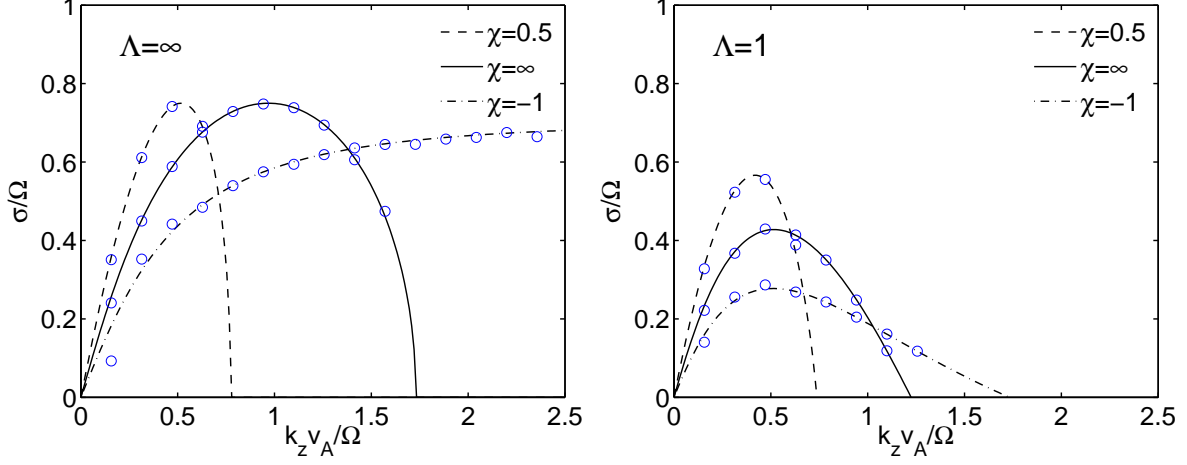


FIG. 9.— Linear dispersion relation of the MRI growth rate with Ohmic resistivity and Hall effect. The growth rate σ is normalized to the orbital frequency Ω^{-1} , and is plotted as a function of $k_z v_A / \Omega$.

where

$$\mathcal{E}_2 = 2k^2 + 1 + \frac{k^2}{\Lambda^2} + \frac{k^2}{2\chi} \left(\frac{2k^2}{\chi} - 3 \right), \quad (\text{B5})$$

$$\mathcal{E}_0 = \frac{k^4}{\Lambda^2} + k^2 \left(k^2 + \frac{2k^2}{\chi} - 3 \right) \left(1 + \frac{1}{2\chi} \right). \quad (\text{B6})$$

Here Λ and χ are the Ohmic and Hall Elsasser numbers defined in (9), based on the background net vertical field B_0 , and k is normalized to Ω/v_A . The Hall Elsasser number χ can have positive or negative signs when the vertical magnetic field B_0 is parallel or anti-parallel to the rotation axis, while Λ is always positive. For pure Hall MRI, the linear dispersion relation above has the property that unstable mode exists only when $1/\chi > -2$ (Wardle 1999), which we will test, though this is not the case for more general perturbations (Balbus & Terquem 2001).

We adopt a very slim simulation box $L_x \times L_y \times L_z = 0.1H \times 0.1H \times 2H$ resolved by $4 \times 4 \times 256$ cells, since we are interested in the vertical wave numbers. Following Sano & Stone (2002a), we initialize the problem with uniform gas density $\rho = 1$ and random velocity perturbations (white noise) on the order of $\delta v = 10^{-6} c_s$. We run the test simulations with given Ohmic and Hall Elsasser numbers as input parameters for about 2.5 orbits. From the simulations we perform Fourier analysis and evaluate the growth rate of v_x for every single vertical mode k_z . In Figure 9, we show the analytical growth rate versus numerical growth rate from our test simulations. Note that the parameter X adopted in Sano & Stone (2002a) corresponds to $2/\chi$ in our case. We have considered parameters with $\chi = 0.5, \infty$ and -1 , corresponding to $X = 4, 0$ and -2 in Sano & Stone (2002a). We see that the numerical dispersion relation agrees very well with analytical results, which proves that our implementation of the Hall term is well suited for conducting simulations in the shearing-box framework.

REFERENCES

- Alexiades, V., Amiez, G., & Gremaud, P. 1996, *Communications in Numerical Methods in Engineering*, 12, 31
- Bai, X.-N. 2011a, *ApJ*, 739, 50
- . 2011b, *ApJ*, 739, 51
- . 2012, PhD thesis, Princeton University
- . 2013, *ApJ*, 772, 96
- Bai, X.-N. & Goodman, J. 2009, *ApJ*, 701, 737
- Bai, X.-N. & Stone, J. M. 2010a, *ApJ*, 722, 1437
- . 2010b, *ApJ*, 722, L220
- . 2011, *ApJ*, 736, 144
- . 2013a, *ApJ*, 767, 30
- . 2013b, *ApJ*, 769, 76
- Balbus, S. A. & Hawley, J. F. 1991, *ApJ*, 376, 214
- Balbus, S. A. & Terquem, C. 2001, *ApJ*, 552, 235
- Birnstiel, T., Klahr, H., & Ercolano, B. 2012, *A&A*, 539, A148
- Blandford, R. D. & Payne, D. G. 1982, *MNRAS*, 199, 883
- Choi, E., Kim, J., & Wiita, P. J. 2009, *ApJS*, 181, 413
- Crutcher, R. M. 2012, *ARA&A*, 50, 29
- D'Alessio, P., Calvet, N., Hartmann, L., Franco-Hernández, R., & Servín, H. 2006, *ApJ*, 638, 314
- Davis, S. W., Stone, J. M., & Pessah, M. E. 2010, *ApJ*, 713, 52
- Desch, S. J. 2004, *ApJ*, 608, 509
- Dong, R., Rafikov, R. R., & Stone, J. M. 2011, *ApJ*, 741, 57
- Ercolano, B. & Glassgold, A. E. 2013, *MNRAS*, 436, 3446
- Ferreira, J. & Pelletier, G. 1995, *A&A*, 295, 807
- Fleming, T. & Stone, J. M. 2003, *ApJ*, 585, 908
- Fleming, T. P., Stone, J. M., & Hawley, J. F. 2000, *ApJ*, 530, 464
- Fromang, S., Latter, H., Lesur, G., & Ogilvie, G. I. 2013, *A&A*, 552, A71
- Gammie, C. F. 1996, *ApJ*, 457, 355
- Garaud, P. 2007, *ApJ*, 671, 2091
- Gardiner, T. A. & Stone, J. M. 2005, *Journal of Computational Physics*, 205, 509
- . 2008, *Journal of Computational Physics*, 227, 4123
- Goldreich, P. & Lynden-Bell, D. 1965, *MNRAS*, 130, 125
- Goodman, J. & Rafikov, R. R. 2001, *ApJ*, 552, 793
- Gressel, O., Nelson, R. P., Turner, N. J., & Ziegler, U. 2013, *ApJ*, 779, 59
- Guilet, J. & Ogilvie, G. I. 2012, *MNRAS*, 424, 2097
- . 2013, *MNRAS*, 430, 822
- Hartmann, L., Calvet, N., Gullbring, E., & D'Alessio, P. 1998, *ApJ*, 495, 385
- Hayashi, C. 1981, *Progress of Theoretical Physics Supplement*, 70, 35

- Hennelbelle, P. & Ciardi, A. 2009, *A&A*, 506, L29
- Hirose, S. & Turner, N. J. 2011, *ApJ*, 732, L30
- Hughes, A. L. H. & Armitage, P. J. 2012, *MNRAS*, 423, 389
- Hull, C. L. H., Plambeck, R. L., Kwon, W., Bower, G. C., Carpenter, J. M., Crutcher, R. M., Fiege, J. D., Franzmann, E., Hakobian, N. S., Heiles, C., Houde, M., Hughes, A. M., Lamb, J. W., Looney, L. W., Marrone, D. P., Matthews, B. C., Pillai, T., Pound, M. W., Rahman, N., Sandell, G., Stephens, I. W., Tobin, J. J., Vaillancourt, J. E., Volgenau, N. H., & Wright, M. C. H. 2014, *ApJ*, submitted
- Ida, S., Guillot, T., & Morbidelli, A. 2008, *ApJ*, 686, 1292
- Igea, J. & Glassgold, A. E. 1999, *ApJ*, 518, 848
- Ilgner, M. & Nelson, R. P. 2006, *A&A*, 445, 205
- . 2008, *A&A*, 483, 815
- Johansen, A., Youdin, A., & Mac Low, M. 2009, *ApJ*, 704, L75
- Joos, M., Hennelbelle, P., & Ciardi, A. 2012, *A&A*, 543, A128
- Kley, W. & Nelson, R. P. 2012, *ARA&A*, 50
- Königl, A., Salmeron, R., & Wardle, M. 2010, *MNRAS*, 401, 479
- Krasnopolsky, R., Li, Z.-Y., & Shang, H. 2011, *ApJ*, 733, 54
- Kretke, K. A. & Lin, D. N. C. 2012, *ApJ*, 755, 74
- Kunz, M. W. & Balbus, S. A. 2004, *MNRAS*, 348, 355
- Kunz, M. W. & Lesur, G. 2013, *MNRAS*, 434, 2295
- Kunz, M. W., Stone, J. M., & Bai, X.-N. 2014, *Journal of Computational Physics*, arXiv:1311.4865
- Latter, H. N., Fromang, S., & Gressel, O. 2010, *MNRAS*, 406, 848
- Lesur, G., Ferreira, J., & Ogilvie, G. I. 2013, *A&A*, 550, A61
- Lesur, G. & Papaloizou, J. C. B. 2010, *A&A*, 513, A60
- Li, Z.-Y. 1996, *ApJ*, 465, 855
- Li, Z.-Y., Krasnopolsky, R., & Shang, H. 2011, *ApJ*, 738, 180
- Lubow, S. H., Papaloizou, J. C. B., & Pringle, J. E. 1994, *MNRAS*, 268, 1010
- Lyra, W. & Klahr, H. 2011, *A&A*, 527, A138
- McElroy, D., Walsh, C., Markwick, A. J., Cordiner, M. A., Smith, K., & Millar, T. J. 2013, *A&A*, arXiv:1212.6362
- Mellon, R. R. & Li, Z.-Y. 2008, *ApJ*, 681, 1356
- Nelson, R. P. & Gressel, O. 2010, *MNRAS*, 409, 639
- Nelson, R. P., Gressel, O., & Umurhan, O. M. 2013, *MNRAS*, 435, 2610
- Okuzumi, S. & Hirose, S. 2011, *ApJ*, 742, 65
- Okuzumi, S., Takeuchi, T., & Muto, T. 2013, *ArXiv e-prints*
- Ormel, C. W. & Okuzumi, S. 2013, *ApJ*, 771, 44
- O’Sullivan, S. & Downes, T. P. 2006, *MNRAS*, 366, 1329
- . 2007, *MNRAS*, 376, 1648
- Paardekooper, S.-J., Baruteau, C., & Kley, W. 2011, *MNRAS*, 410, 293
- Pandey, B. P. & Wardle, M. 2012, *MNRAS*, 3001
- Perez-Becker, D. & Chiang, E. 2011a, *ApJ*, 735, 8
- . 2011b, *ApJ*, 727, 2
- Petersen, M. R., Stewart, G. R., & Julien, K. 2007, *ApJ*, 658, 1252
- Pinilla, P., Birnstiel, T., Ricci, L., Dullemond, C. P., Uribe, A. L., Testi, L., & Natta, A. 2012, *A&A*, 538, A114
- Preibisch, T., Kim, Y., Favata, F., Feigelson, E. D., Flaccomio, E., Getman, K., Micela, G., Sciortino, S., Stassun, K., Stelzer, B., & Zinnecker, H. 2015, *ApJS*, 160, 401
- Raettig, N., Lyra, W., & Klahr, H. 2013, *ApJ*, 765, 115
- Ribas, Á., Merín, B., Bouy, H., & Maud, L. T. 2013, *ArXiv e-prints*
- Salmeron, R., Königl, A., & Wardle, M. 2011, *MNRAS*, 412, 1162
- Sano, T. & Stone, J. M. 2002a, *ApJ*, 570, 314
- . 2002b, *ApJ*, 577, 534
- Santos-Lima, R., de Gouveia Dal Pino, E. M., & Lazarian, A. 2012, *ApJ*, 747, 21
- Seifried, D., Banerjee, R., Pudritz, R. E., & Klessen, R. S. 2012, *MNRAS*, 423, L40
- Shakura, N. I. & Sunyaev, R. A. 1973, *A&A*, 24, 337
- Shi, J., Krolik, J. H., & Hirose, S. 2010, *ApJ*, 708, 1716
- Sicilia-Aguilar, A., Hartmann, L., Calvet, N., Megeath, S. T., Muzerolle, J., Allen, L., D’Alessio, P., Merín, B., Stauffer, J., Young, E., & Lada, C. 2006, *ApJ*, 638, 897
- Simon, J. B., Bai, X.-N., Armitage, P. J., Stone, J. M., & Beckwith, K. 2013a, *ApJ*, 775, 73
- Simon, J. B., Bai, X.-N., Stone, J. M., Armitage, P. J., & Beckwith, K. 2013b, *ApJ*, 764, 66
- Simon, J. B., Hawley, J. F., & Beckwith, K. 2011, *ApJ*, 730, 94
- Stapelfeldt, K. R., Ménard, F., Watson, A. M., Krist, J. E., Dougados, C., Padgett, D. L., & Brandner, W. 2003, *ApJ*, 589, 410
- Stone, J. M. & Gardiner, T. A. 2010, *ApJS*, 189, 142
- Stone, J. M., Gardiner, T. A., Teuben, P., Hawley, J. F., & Simon, J. B. 2008, *ApJS*, 178, 137
- Suzuki, T. K. & Inutsuka, S.-i. 2009, *ApJ*, 691, L49
- . 2013, *ArXiv e-prints*
- Takeuchi, T. & Okuzumi, S. 2013, *ArXiv e-prints*
- Tomida, K., Tomisaka, K., Matsumoto, T., Hori, Y., Okuzumi, S., Machida, M. N., & Saigo, K. 2013, *ApJ*, 763, 6
- Turner, N. J., Fromang, S., Gammie, C. F., Lesur, G., Wardle, M., & Bai, X.-N. 2014, in *PPVI*, ed. C. P. Dullemond No. arXiv:1401.7306
- Turner, N. J. & Sano, T. 2008, *ApJ*, 679, L131
- Turner, N. J., Sano, T., & Dziourkevitch, N. 2007, *ApJ*, 659, 729
- Urpín, V. 2003, *A&A*, 404, 397
- Walsh, C., Millar, T. J., & Nomura, H. 2010, *ApJ*, 722, 1607
- Walsh, C., Nomura, H., Millar, T. J., & Aikawa, Y. 2012, *ApJ*, 747, 114
- Wardle, M. 1997, in *Astronomical Society of the Pacific Conference Series*, Vol. 121, IAU Colloq. 163: Accretion Phenomena and Related Outflows, ed. D. T. Wickramasinghe, G. V. Bicknell, & L. Ferrario, 561
- Wardle, M. 1999, *MNRAS*, 307, 849
- . 2007, *Ap&SS*, 311, 35
- Wardle, M. & Königl, A. 1993, *ApJ*, 410, 218
- Wardle, M. & Salmeron, R. 2012, *MNRAS*, 422, 2737
- Weidenschilling, S. J. 1977, *MNRAS*, 180, 57
- Wolk, S. J., Harnden, Jr., F. R., Flaccomio, E., Micela, G., Favata, F., Shang, H., & Feigelson, E. D. 2005, *ApJS*, 160, 423
- Yang, C.-C., Mac Low, M.-M., & Menou, K. 2012, *ApJ*, 748, 79
- Youdin, A. N. 2011, *ApJ*, 731, 99